UQAC

Université du Québec
à Chicoutimi

MEMOIRE PRESENTÉ À
L'UNIVERSITÉ DU QUÉBEC À CHICOUTIMI

COMME UNE EXIGENCE PARTIELLE
DE LA MAÎTRISE EN INGÉNIERIE

PAR
MOHAMED ATTIA

"ÉTUDE DE LA CONCEPTION ET LE TRAITEMENT
THERMIQUE D'UN BRAS DE SUSPENSION D'AUTOMOBILE EN
ALLIAGE D'ALUMINIUM A357 SEMI-SOLIDE"

DECEMBRE 2019

UNIVERSITY OF QUEBEC AT CHICOUTIMI

THESIS PRESENTED TO
THE UNIVERSITY OF QUEBEC AT CHICOUTIMI

IN PARTIAL FULFILLMENT OF THE REQUIREMENTS FOR
THE DEGREE OF MASTER OF SCIENCES IN ENGINEERING

BY
MOHAMED ATTIA

"STUDY OF DESIGN AND THERMAL TREATMENT OF
AUTOMOTIVE CONTROL ARM FABRICATED FROM A357
SEMI-SOLID ALLOY"

DECEMBER 2019

Résumé

Le développement de composants mécaniques automobiles plus légers et plus solides a un effet marqué sur la sélection judicieuse des métaux éligibles et sa conception dans la fabrication moderne. Les métaux légers et alliages d'aluminium sont connus pour leur résistance élevée qui en fait des matériaux de choix dans la fabrication de composants mécaniques dynamiques pour les automobiles. Le moulage semi-solide est considéré comme une technique efficace pour produire des alliages d'aluminium de qualité et de performances supérieures par rapport aux techniques de moulage traditionnelles.

Le bras de suspension inférieur du système de suspension automobile est le composant mécanique chargé de relier les roues du véhicule au châssis. Il fait partie de la masse non suspendue du véhicule, et son poids léger est d'une grande importance pour augmenter l'efficacité du véhicule et réduire sa consommation de carburant. Une nouvelle tendance est de fabriquer cette pièce à partir d'alliages d'aluminium en raison de sa légèreté, de son haut rapport de résistance/poids et de sa meilleure résistance à la corrosion que l'acier.

La présente étude porte sur la conception et le développement d'un bras de suspension inférieur admissible fabriqué à partir d'alliages semi-solides en aluminium A357.0 utilisant la technique de Rhéocasting SEED (Swirled Equilibrium Enthalpy Device). Ce travail de recherche porte sur l'étude de cycles de traitement thermique innovants pour améliorer les propriétés mécaniques de résistance et de fatigue de l'alliage étudié. Cette étude vise également à examiner les paramètres de conception du bras de suspension et à proposer une

conception innovante plus légère et plus efficace que la conventionnelle. Enfin, la durée de vie en fatigue et les performances du bras de suspension sont étudiées pour les cycles de traitement thermique spécifiques appliqués aux pièces examinées du bras de suspension. Les résultats révèlent des performances mécaniques supérieures en termes de résistance, de ductilité et de résistance à la fatigue du cycle de vieillissement WC3 par rapport aux conditions T6 standard. Les résultats des tests de fatigue montrent une durée de vie doublée en fatigue du cycle de vieillissement WC3 par rapport à la condition T6. D'un autre côté, la conception en treillis modifiée s'est avérée offrir une meilleure répartition des contraintes et une contrainte Von-Mises plus faible que la conception conventionnelle. La conception modifiée est également plus légère que la conception conventionnelle, ce qui la rend plus efficace pour une utilisation dans les applications automobiles.

Abstract

The development of lighter and stronger automotive mechanical components has a marked effect on the judicious selection of qualifying metals and its design in modern manufacturing. Aluminum light metals and alloys are known of its high specific strength which makes them materials of choice preferable in the manufacturing of automotive dynamic mechanical components. The semisolid casting (or semisolid forming SSF) is considered as an effective technique for producing aluminum alloys of superior quality and performance compared to traditional casting techniques.

The lower control arm in automotive suspension system is the mechanical component responsible of linking the wheels of the vehicle to the chassis. It is a part of vehicle unsprung mass, and its lightweight is of great importance to increase vehicle efficiency and decrease its fuel consumption. A new trend is to manufacture this part from Aluminum alloys due to its lightweight, high specific strength and better corrosion resistance than steel.

This current study deals with the design and development of qualifying lower control arm manufactured from A357.0 Aluminum semi solid alloys using SEED (Swirled Equilibrium Enthalpy Device) Rheocasting technique. This research work covers the study of innovative heat treatment cycles for enhancing the strength and fatigue mechanical properties of the alloy investigated. This study also aims at investigating the design parameters of control arm and proposing an innovative design which is lighter and more efficient than conventional one. Finally, the fatigue life and performance of the control arm are studied for the specific heat treatment cycles applied on applicable control arm parts investigated. The results reveal superior mechanical performance regarding strength, ductility and fatigue life of the aging

cycle WC3 compared to standard T6 conditions. The results of fatigue testing show double fatigue life of the aging cycle WC3 compared to T6 condition. On the other hand, the modified trussed design has proven to provide better stress distribution and lower Von-Mises stress than the conventional design. The modified design is also lighter than the conventional design, making it more efficient for the use in automotive applications.

<u>Acknowledgments</u>

<u>Publications</u>

Four publications in the form of journal articles, conference paper and posters were prepared

in the fulfillment of this master's degree. Details of each publication are illustrated below:

<u>Scientific papers</u>

1. M.Attia, K.Ragab, M. Bouazara and X-G.Chen, "Influence of thermal treatment and design parameters on the fatigue life of automotive control arm fabricated from A357 semi-solid alloy", TMS conference, USA, 2020. **(Accepted for publication).**

2. M.Attia, K.Ragab, M. Bouazara and X-G.Chen, "Effect of multi-step thermal aging and design parameters on the total fatigue life of aluminum A357 semisolid casted automotive suspension control arm", **(Draft to be submitted)**

<u>Scientific posters</u>

1. M.Attia, K.Ragab, M. Bouazara and X-G.Chen, "On the materials performance of Aluminum semi-solid alloys subjected to various thermal aging parameters", REGAL, McGill University, Quebec, Canada, 2018.

2. M.Attia, K.Ragab, M. Bouazara and X-G.Chen, "Study of design and thermal treatment of automotive control arm fabricated from A357 semi-solid alloy", REGAL, Laval University, Quebec, Canada, 2019.

Contents

List of Figures

List of tables

Chapter I

Introduction

1. Introduction

Aluminum has become one of the most popular metals that are widely used in many engineering applications. It is characterized by its high strength-to-weight (or specific strength) ratio which is one of the most important criteria in material selection. Specific strength of the Aluminum alloy 6061-T6 is 115 kN.m/kg compared to 46.4 kN.m/kg for the popular low carbon steel AISI 1010 [1–3]. This property made Aluminum of much interest in automotive industry where light materials are of great importance to increase efficiency and decrease fuel consumption. Figure 1.1 shows a market research by Ducker Worldwide [4] representing the net pound of Aluminum used per vehicle from 1975 to 2015. It can be observed that the use of Aluminum in 2015 is more than 4 times its use in 1975. The study extrapolates the trend and predicts the use of Aluminum in automotive industry; it will reach more than 550 pounds/vehicle by the year 2028. This study highlights the current trend of automotive industry to move from ferrous alloys to aluminum alloys in the production of modern vehicles. Aluminum also possesses superior corrosion resistance properties compared to steel; a layer of aluminum oxide is formed on the surface of aluminum alloys that stops further oxidation of aluminum. This property makes the mechanical part that is made from aluminum alloys lasts longer than its rivals made from steel or ferrous alloys. As a result, aluminum mechanical parts that are subjected to dynamic loading may have longer fatigue life than those made of ferrous alloys, although steel possesses infinite fatigue life below certain stress levels. Thus, the two major problems in ferrous alloys which are corrosion and heavy weight are solved by using aluminum alloys. There is no doubt that steel

is one of the most common materials having very high strength and ductility compared to aluminum. However, as mentioned earlier, in the design field what cares most is the strength-to-weight ratio and not only strength. Therefore, aluminum outperforms steel in this particular property making the use of aluminum very favorable for mechanical designers. One of the advantages of aluminum over steel is also its castability. Aluminum melting point is around 660 °C compared to cast irons that is around 1300 °C which makes the use of aluminum is more economical and safer to handle than cast irons. Many mechanical components are produced by direct casting of aluminum, while others are machined after casting to produce the desired surface finish and shape [5]. Aluminum is also used in the manufacturing of some high-end vehicles interior including the dashboards to limit noise and ticking resulted from vibrations due to quality of the road. So, aluminum can be considered as a bridge material between traditional ferrous alloys and new high-end composites as carbon fibers which are used recently in the production of high-end racing cars and Formula One cars.
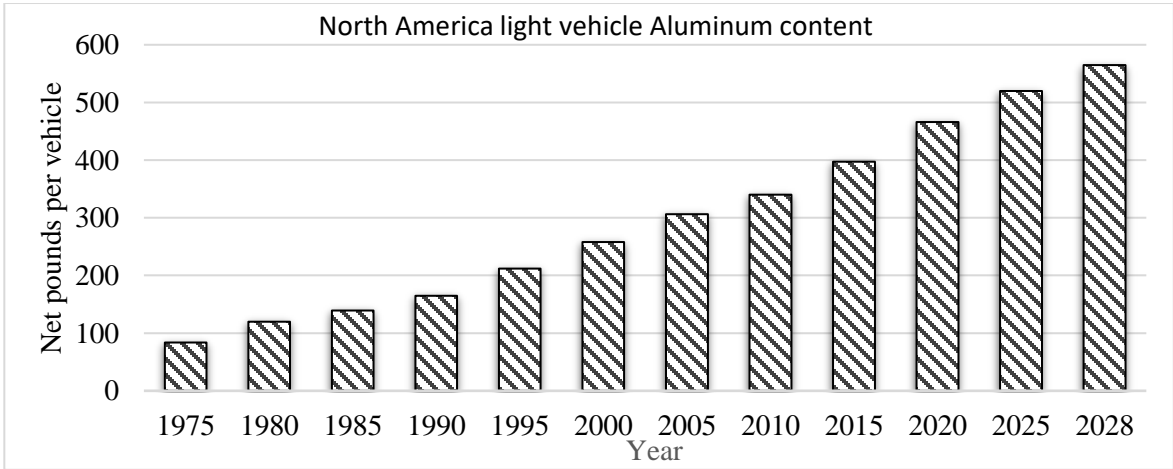
Figure 1.1:   Net pounds of Aluminum per vehicle over years [4].

One of the important mechanical components that is manufactured from Aluminum alloys is the lower control arm in automotive [6]. This mechanical component has a major role in the suspension kinematics of the car, it can also carry the weight of the car in some designs. It is important for this part to possess high strength to preserve its functional perfection, but also, acceptable ductility to withstand shocks and vibrations from the road [7]. The material selection of this mechanical component as well as the geometric shape has been the matter of research in the recent studies. Suspension control arms are subjected to continuous cyclic loading due to the acceleration and deceleration actions of the vehicle [8]. As a result, the expected type of failure for this part is the fatigue failure.

This research work aims at studying the automotive control arm regarding its design and material characteristics. The study aims in the enhancement of the design and fatigue performance of the A357 semi-solid control arm preserving its original dimensions.

First chapter outlines an introduction of the control arm regarding its types, functions and different designs. Furthermore, this part focuses on the characteristics of suspension control arm regarding its geometrical shape, type, material and manufacturing technique applied.

Second chapter of the literature review starts brief discussion on introduction to aluminum casting alloys and its designation. Following that, an explanation of the new semi-solid casting technique focusing on using the Swirled Equilibrium Enthalpy Device (SEED) technology with the A357 alloy. Thereafter, a highlight on the effect of semi-solid casting on the mechanical and microstructural characteristics, as well as, the advantages and disadvantages of semi-solid casting are presented. Moreover, this part outlines a discussion

of previous studies on the effect of multiple thermal aging on the mechanical and microstructural properties of aluminum alloys. Finally, it presents previous trials applied to enhance and optimize the design of the control arm, which will be used in the development of the modified design in this project.

Third and fourth chapters concern the methodology and results respectively, in which the experiments applied in this project as well as the results are discussed.

Finally, the conclusions drawn from this work are reported at the last chapter including the most significant results concerning the innovative aging cycles, as well as, the modified design and its effect on the total fatigue life.

1.1 Aluminum casting alloys

Aluminum comes as the most common non-ferrous metal in the world. The annual consumption is around 24 million tons in which 75% of this volume –around 18 million tons– is extracted from ore "primary Aluminum". The remaining 25% comes from recycled Aluminum scrap [1]. The first real market for Aluminum was castings after the commercializing of Aluminum production by the Hall–Héroult process[1]. The use of Aluminum first was limited to simple products as combs, hand mirrors, hat pins and women's accessories. The introduction of the Aluminum cooking pans then was widely welcomed to

---

[1] Hall–Héroult process is the process of smelting Aluminum used majorly in industry. It involves the use of bauxite dissolving its Aluminum oxide (Alumina) to produce Aluminum by electrolyzing the molten salt bath[1].

replace the old cast iron and brass pots. By the end of the 19th century, the cost of Aluminum steadily decreased. This made it economical to use in engineering applications. Three very important markets considered using Aluminum: Electrification –to use as conductor wires–, automotive parts –where light weight was important– and aviation, when the Wright brothers made the first controlled airplane with many parts made from Aluminum. The engineering use of Aluminum opened the door for developing alloys with enhanced properties [9,10].

1.1.1 Advantages and limitations of aluminum castings

Aluminum castings are produced from many types of aluminum alloys. Over 100 compositions are registered, and more than 300 alloys are globally used. Pure aluminum is classified into two main categories: extreme purity and commercial purity. Table 2.1 shows the ISO designation of pure aluminum [1,9].

Table 1.1:   Classification of Aluminum based on International Standard (ISO) [1].

Purity of aluminum	Designation
Extreme purity	A199.99R; A199.95R; A199.9R; A199.8; A199.7
Commercial purity	A199.8; A199.7; A199.5
For electrical industry (wires)	A199.4; A199.0; A198 E-Al
Extreme purity	A199.99R; A199.95R; A199.9R; A199.8; A199.7; A199.5
Commercial purity	E-Al*
For electrical industry (wires)	E-Al**

* Electrical conductivity in annealing condition is more than $35.7\ \mu\mathrm{Ohm} \times \mathrm{mm}^{-2}$
** Electrical conductivity in annealing condition is more than $35.4\ \mu\mathrm{Ohm} \times \mathrm{mm}^{-2}$

Aluminum as a pure form is not used in engineering application. Alloying elements should be added to enhance the mechanical characteristics of this soft metal. Below (Table 2.2) is the range of physical and mechanical properties of aluminum alloys used in industry.

Table 1.2:   Physical and mechanical properties of aluminum alloys [9].

Tensile strength, ksi (MPa)	10–72 (70–505)
Yield strength, ksi (MPa)	3–65 (20–455)
Elongation, %	<1–30
Hardness, HB	30–150
Electrical conductivity, %IACS	18–60
Thermal conductivity, Btu · in./h · ft^2 · °F at 77 °F (W/m · K at 25 °C)	660–1155 (85–175)
Fatigue limit, ksi (MPa)	8–21 (55–145)
Coefficient of linear thermal expansion at 68–212 °F (20–100 °C)	9.8–13.7 × 10^{-6}/°F (17.6–24.7) × 10^{-6}/°C)
Shear strength, ksi (MPa)	6–46 (42–325)
Modulus of elasticity, 10^6 psi (GPa)	9.5–11.2 (65–80)
Specific gravity	2.57–2.95

Some advantages of aluminum alloys over other metals are [9]:

- Multiple welded assemblies can be replaced with single cast part.

- Less machining.

- Can be casted by every know process offering wide range of productivity, volume, quality and machinability.

- Possesses very good fluidity for casting thin and fine sections.

- Have lower melting temperature than other metals (ex. Steel) making it easier to cast.

- Casting process can be highly automated for mass production.

However, Aluminum castings can have some limitations as thin sections may sometimes be difficult to be casted. For complex geometric shapes solidification can result in surface discontinuities and varying internal microstructure characteristics [2,9,11].

1.1.2 Alloying elements used in Aluminum alloys

Alloying elements are used to enhance the mechanical properties of aluminum alloys. These alloying elements include: Copper, Silicon, Magnesium, zinc and tin. Other elements can be found within the aluminum cast as iron [9,12].

1.1.3 Designation

Many standards are found in aluminum designation. The most widely used system in the United States is the Aluminum Association (AA).

1.1.3.1 The Aluminum Association (AA) Alloy designation system

There are four digits in the AA designation, the meaning of the digits are as follows:

- First digits: Principle alloying constituent(s).

- Second and third digits: Specific alloy designation (meaningless number specific for each alloy).

- Fourth digit: for casting is '0' and for ingot is '1, 2'.

When the variation in composition is so low; the designation is indicated by a preceding letter (A, B, C, etc.). For example, the first version of alloy 356.0 will be A356.0, the second will be B356.0 and so on [12,13]. Listed below are the categories of the first digit of Aluminum designation:

- lxx.x, pure aluminum (99.00% or greater)

- 2xx.x, aluminum-copper alloys

- 3xx.x, aluminum-silicon + copper and/or magnesium

- 4xx.x, aluminum-silicon

- 5xx.x, aluminum-magnesium

- 7xx.x, aluminum-zinc

- 8xx.x, aluminum-tin

- 9xx.x, aluminum + other elements

- 6xx.x, unused series

1.1.3.2   AA Casting Temper Designation System

For the heat treatment type there are the following letters –or letters with numbers– to indicate the type of treatment.

- F, as-cast.

- O, annealed.

- T4, solution treated and aged.

- T5, precipitation hardened.

- T6, solution heat treated, quenched, and precipitation hardened.

- T7, solution heat treated, quenched, and over-aged.

1.2   Aluminum Casting Techniques

One of the advantages of Aluminum alloys is its wide castability properties. The following casting techniques can be used for producing Aluminum casting alloys.

- Expandable mold gravity-feed casting processes

  - Sand casting

  - Lost-foam pattern casting

  - Shell mold casting

  - Plaster casting

  - Investment casting

- Nonexpendable (permanent) mold gravity feed casting processes

  - Permanent mold casting

  - Low-pressure die casting

  - Vacuum riserless casting (VRC)

  - Centrifugal casting

  - Squeeze casting

  - Semi-solid forming

Semi-solid casting is considered as the casting technique of interest in this project and is the one used in the manufacturing of the automotive control arm [5,14].

1.3   Lower control arm in automotive industry

Suspension system of vehicles is the assembly of mechanical components located between the frame (or body) of the vehicle and road wheels. The suspension system is responsible of providing four main tasks in the vehicle:

   a.   Absorbing of shocks from road: provides passengers comfort, vehicle stability and handling.

   b.   Maintaining contact between vehicle tires and road under different topographies and road conditions.

   c.   Transmitting engine power (power applied to vehicle wheels) to the chassis in the form of acceleration and braking forces.

   d.   Maintaining proper geometry and kinematics of road wheels during driving and cornering.

Thus, it can be observed the impact of suspension systems in the overall performance of vehicles [15]. Car manufacturers invest large capitals in the development of suspension systems as it is one of the most important systems regarding safety and performance of automotive. Suspension systems consist of three main parts:

   a.   Road springs.

   b.   Dampers.

   c.   Suspension linkage.

Springs and dampers are responsible of the response of the vehicle under random excitations from different road conditions. They are the matter of research in many automotive vibration studies, aiming at selecting the best spring and damper constant for optimum driving

experience. On the other hand, the suspension linkages are the assembly of mechanical components linking the whole suspension system and transmitting force to the chassis of the vehicle [7,15].

The lower control arm is a major mechanical component in automotive suspension linkage system. It is responsible of transferring vehicle load to the ground and maintaining the kinematic motion of the wheel. Figure 1.2 shows the suspension assembly of a supporting type control arm showing its function in vehicle suspension [16].
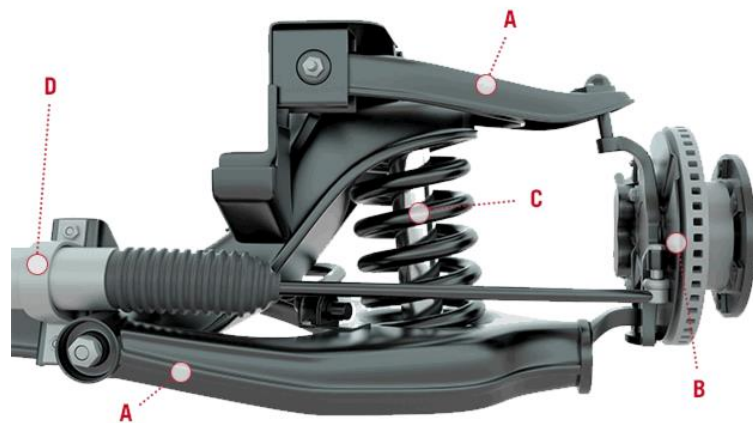
Figure 1.2:   Automotive suspension system. A) Control arms. B) Wheel spindle. C) Spring-damper assembly. D) Rack and pinion assembly [16].

To better explain the functions and importance of control arm in vehicle suspension; suspension arms can be categorized in terms of functionality into two main different functions. It can also be categorized into three main different designs of suspension control arms; each has its advantages and disadvantages. Functions and designs of control arms are discussed in the following two subsections.

1.4   Function of suspension control arm

Suspension control arms are divided into two categories in terms of function each has its own shape and design:

- Guiding type control arm.

- Supporting type control arm.

Guiding type control arms, shown in Figure 1.3a, is responsible for reserving the kinematic location of the wheel. The weight of the vehicle is transmitted through the spring-damper assembly to the wheel spindle bearing then to the ground. It does not support the weight of the vehicle; it supports mainly the load induced by acceleration and braking. One popular suspension assembly that uses guiding type control arm is called the MacPherson strut suspension assembly that is the most widely used in commercial cars.

Supporting type control arm shown in Figure 1.3b is responsible for supporting the weight of the vehicle as well as maintain the kinematics of suspension. The spring-damper rests on a special location on the control arm where the weight is transmitted from the control arm to the spindle bearing then to the ground [15–17].
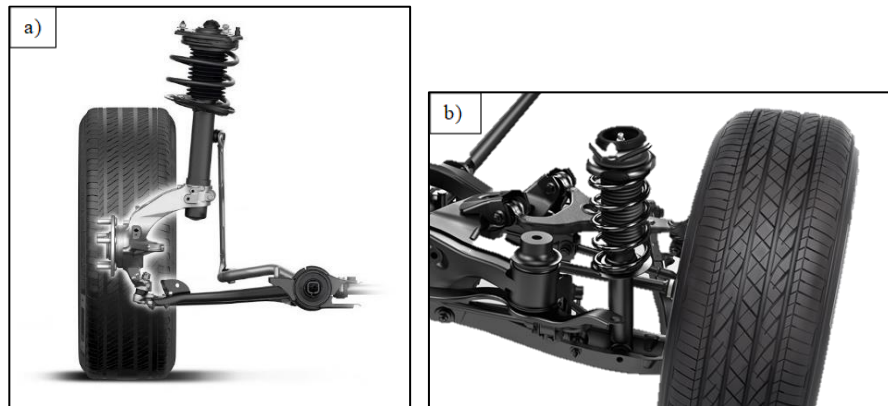
Figure 1.3: Different functions of control arm a) guiding type, b) supporting type control arm [16].

These designs are found in the independent suspension, in which the two wheels can move freely to each other as shown in Figure 1.4a. This type is usually found in the front suspension of front wheel drive cars. While Figure 1.4b represents a rigid axle suspension (torsion bar suspension) which is very common in the rear axle suspension of front wheel drive vehicles. This type of suspension system is not of interest in this project as it is completely different from the independent suspension.
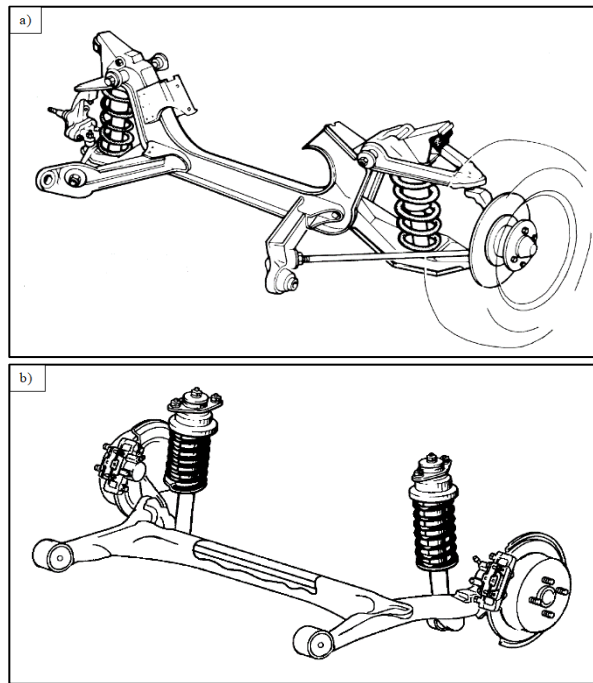
Figure 1.4:   Different forms of suspension systems. a) Independent suspension, b) rigid axle suspension [15].

1.5   Design of suspension control arm

Suspension lower control arms can be manufactured into three different designs:

- Press-in lower control arm.

- Bolt-in lower control arm.

- Unitized lower control arm.

The press-in design of control arm, shown in Figure 1.5a, is when the ball joint is pressed in the body of the control arm. This allows the ball joint to be changed without the need to change the whole control arm if it is damaged.

The bolt-in design shown in Figure 1.5b allows the bolt joint to be bolted to the control arm body. The change of the ball joint will result in misalignment and the vehicle will need realignment.

The last design is the unitized design shown in Figure 1.5c; it is that where the ball joint socket is machined (or casted) in the body of the control arm. The damage of the ball joint will need the change of the whole control arm.

Figure 1.5:   Different designs of control arm a) Press-In, b) Bolt-In and c) Unitized [16].

Complete understanding of the importance and functions of different types of suspension systems helps in applying the proper loads to the suspension arm in this study. Suspension control arm of interest in this study is explained in the next subsection.

1.6   A357.0 semisolid casted lower control arm

The control arm, shown in Figure 1.6, is part of interest in this project. It is a guiding type control arm with unitized design. It is subjected to dynamic loads that results from acceleration and deceleration of the vehicle. The expected type of failure is fatigue failure as a result of the dynamic loadings.

Figure 1.6:   Conventional A357.0 semisolid casted lower control arm

1.7   Objective and project sequence

The objective of the project is to enhance the fatigue performance of this control arm as well as the design preserving its basic dimensions. The project goes into two parallel ways; the first is to develop a new heat treatment method instead of the traditional T6. The second, is to develop a better design that enhances the stress distribution and decreases the weight of this applicable part. Different design approaches are applied in order to accomplish these design modifications. Literature of optimized design of different types of control arm was used in the development of the renovated design. Finally, analytical calculations are discussed to expect the total enhancement of the part's fatigue life by the application of both the renovated design, as well as, the best thermal aging.

Chapter II

Literature review

2. Literature review

2.1 A357.0 Casting Alloy

From the previous designation system, it can be noted that A357.0 is an Aluminum-Silicon-Magnesium alloy and is a variation to the 357.0 alloy. The composition of the alloy is listed in Table 2.1.

Table 2.1:   A357.0 alloy chemical composition.

Composition, Wt%						
Si	Fe	Cu	Mn	Mg	Zn	Ti
6.5-7.5	0.2	0.2	0.1	0.4-0.7	0.1	0.04-0.2

The A357 alloys processes high Mg contents and is characterized by the formation of π-Fe intermetallic phases compared to the A356 alloys. The increased Mg content enhances the fatigue properties of the alloy [18]. A357 is known for its sensitivity of natural aging; therefore, it should maintained at low temperatures to avoid natural aging in the period between solution heat treatment and artificial aging [19].

The A357.0 casting alloy is preferable in the high strength automotive casted components. It is also widely used in aerospace and military applications due to its superior weldability, castability, high strength and corrosion resistance [20]. The most common thermal treatment applied to this alloy is the T6 thermal treatment. This thermal aging cycle provide the material with the required strength and ductility for the use in industry. The T6 thermal treatment consists of solution heat treatment at 540 °C for 8 h, then quenched in water maintained at 60 to 80 °C, followed by artificial aging at 175 °C for 7 h. Following artificial

aging the alloy can be left to natural aging at room temperature for 4 to 12 h [21]. The solution heat treatment is essential in this alloy to dissolve the Mg and Si which are segregated in the primary Al in the as-cast alloy. Quenching then stops any precipitation reaction during cooling, while water at around 60-80 °C is preferable to decrease the residual stress in the material improving fatigue life [22].

2.2 Semi-solid casting process

Semi-solid forming (SSF) also known as Semi-solid metallurgy (SSM) is a forming technique invented by David Spencer in 1971 as a part of his doctoral thesis [23]. Semisolid forming combines the processes of casting, forming and extrusion. Regarding this forming process, force is applied –either mechanical or electromagnetic– to fragment the semisolid structure in the liquidus-solidus range. The temperature is retained above melting point for the whole process, then the semisolid paste is compressed inside the mold cavity under high pressure to take its final geometry [24]. Thus, turbulence associated with gravity pouring or injection is minimized; reducing internal porosity significantly as it reduces the volume of solidifying liquid [9]. Figure 2.1 shows aluminum billet in the semi-solid state ready for high pressure die casting that follows the semi-solid state. The laminar flow of the semisolid forming process is considered the main advantage of the SSM processes on other normal casting techniques. The laminar flow decreases the formation of oxides and gas entrapment and shrinkage during solidification; preventing blistering during heat treatment. Therefore, SSM casts can undergo aging heat treatment that increases the tensile and yield strength without decreasing the ductility so much [25].
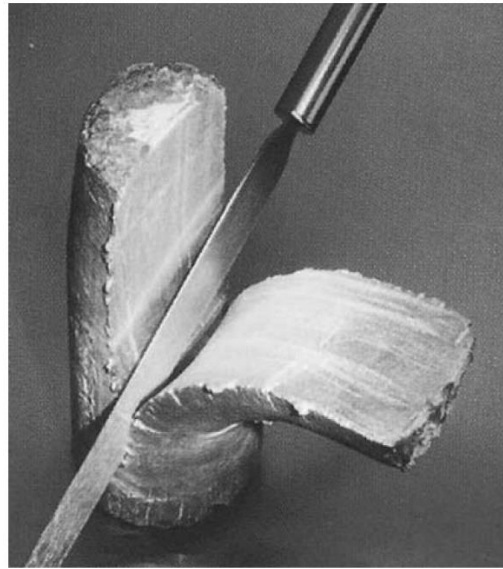
Figure 2.1:   Aluminum billet in the semi-solid state (Courtesy of formcast, Inc.) [11].

One of the characteristics of semi-solid metal working is the high casting pressure, for illustration, Figure 2.2 shows different casting techniques with its pressure and gate velocity. It is noticed that semi-solid casting has relatively high pressure and lower gate velocity than all other casting techniques.
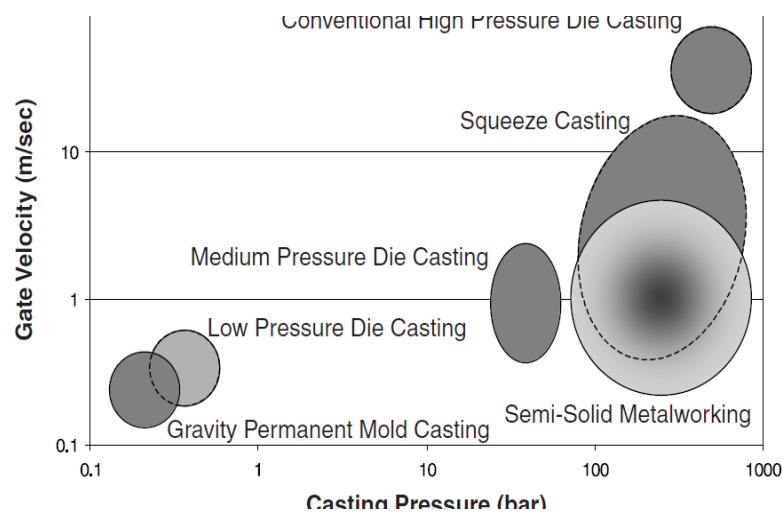
Figure 2.2:   Comparison of casting pressures and gate velocities for numerous die casting processes.

The laminar flow speed varies from 20 to 50 cm/s since SSF has about 70% solid; therefore, the only expected shrinkage porosity is micro-porosity that can occur if the compressive force is not enough [24]. Table 2.2 shows the solidification range of some aluminum casting alloys to be in the semi-solid state which is essential to maintain during semi-solid casting process [11]. The major advantages of semi-solid metal working over the conventional die can be summarized by these three points:

- Reduction of entrapped gasses

- Reduction of solidification shrinkage

- Modification of microstructure

Table 2.2:   Freezing ranges for common die cast Aluminum alloys.

Aluminum Alloy Designation	Approximate Solidification Range (°C)
319	604–516
356	613–557
357	613–557
380	593–538
383	582–516
390	649–507

2.2.1   Managing gases and shrinkage in the die

Due to high viscosity of semi-solid metal; SSM exhibits planar metal flow combined with large gate cross-sectional area and slow shot speeds compared to conventional die casting. This also allows gases to escape from the die before compression of gases. The term laminar flow that is always used with SSM is not completely true. The high flow rates despite the high viscosity of SSM causes the flow to be turbulent at some parts. However, this turbulence does not cause gas entrapment inside the metal but occurs at the metal fill front [11].

As SSM is partially solid, thus, shrinkage porosity is minimized. Also, the amount of heat that should be removed to cause solidification is reduced. Therefore, cycle times of SSM is much less than traditional die casting and at the same time reduces thermal cycles of the die resulting in a higher lifetime of the die [11].

2.2.2 Microstructure evolution due to semi-solid metal working

Products manufactured using SSM does not have the dendritic structure as that manufactured by traditional die casting. The dendritic structure is broken up during processing and changes to spheroidal/equiaxed grain structure. The equiaxed structure exhibits superior mechanical properties that can rivals the products made by forging [11].

 There are two feasible routes for SSM named "Rheocasting" (direct SSM) and "Thixocasting" (indirect SSM). It is still not clear which of these two routes may be of greater significance in the future. "Thixocasting" it involves the formation of the required billets with desired microstructure from continuous casting which is obtained usually by electromagnetic stirring. It has some disadvantages as the electromagnetically stirring process can sometimes produce inhomogeneous billets. Also, there is lost metal in reheating for about 10% of the total weight. Gates and risers cannot be recycled in the forming facility but must be sent back to ingot producer. As well as, total cycle time is high and can increase the part cost. For "Rheocasting" liquid metal is poured in an equal size container with the die to be filled and is then fed to the die chamber. This avoids the reheating process of stock metal. The SSM mix is produced and injected on demand which decrease the total cycle time and thus cost. The desired structure is obtained by cooling, grain refinement and stirring [11],

[23,24]. Figure 2.3 shows the comparison between microstructure of (a) direct semi-solid metalworking, (b) indirect semi-solid metalworking and (c) conventional casting processes.
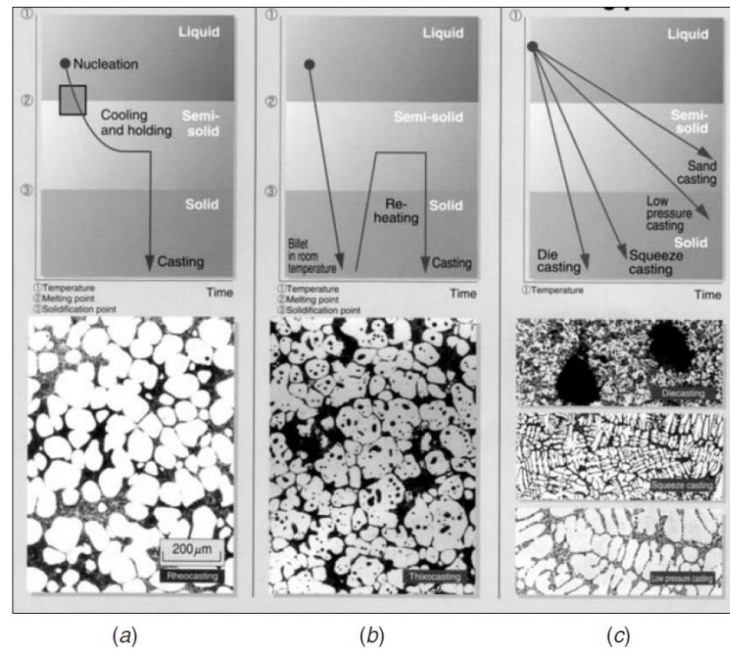
Figure 2.3:　Process comparison (a) Rheocasting process, (b) Thixocasting process and (c) conventional casting process (Courtesy of UBE Machinery, Inc).

The semisolid casting process is characterized by the presence of equiaxed (or rosettes like) grain structure. It differs than the dendritic structure found in conventional casting as shown in Figure 2.4. It can also be observed that the microstructure of semisolid casting is nearly the same throughout the whole thickness as shown in Figure 2.4b,c [26].
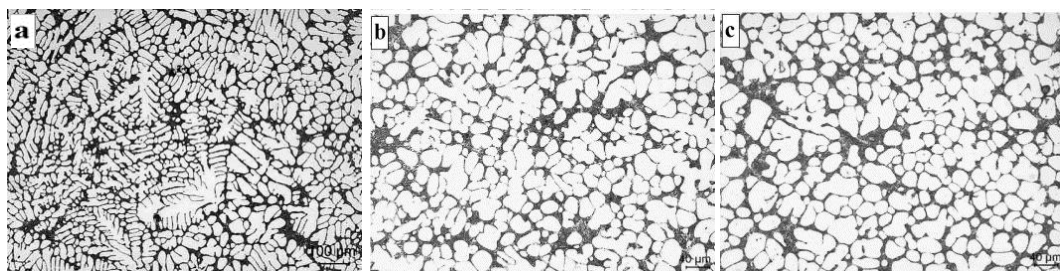
Figure 2.4:　Microstructure of A357 a) conventional casting, b) semisolid casting halfway between the edge and center, c) semisolid at the center of the ingot [26].

Figure 2.5 shows the effect of semisolid casting in fragmenting the β-Fe intermetallics and spherodizing the π-Fe and silicon. The sample was taken from the control arm and polished to be used under the scanning electron microscope.
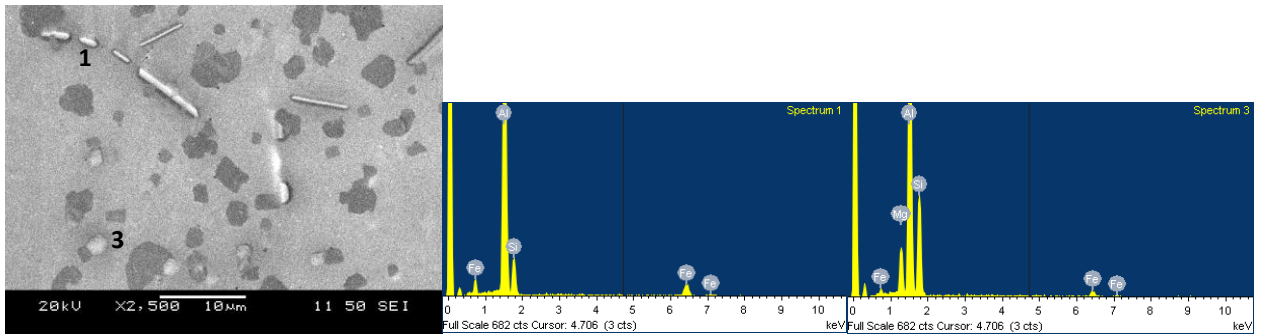
Figure 2.5:   SEM imaging of A357 semisolid.

2.2.3   Advantages of semi-solid metal working

Semi-solid metal working (SSM) improves the mechanical properties of the casted component significantly over traditional casting. Many major problems found in conventional casting are eliminated by only using the semi-solid casting technique. Some of the advantages and characteristics of semi-solid casting over conventional casting techniques are [23]:

- Lower heat content than liquids
    - Higher forming speed
    - Less mold erosion
    - Forming of higher melting point materials
    - Ferrous metal forming
    - Forming of reactive materials
- Presence of solid during mold filling

- o Less shrinkage porosity

- o Require less feeding

- o Less macrosegregation

- o Fine grain structure

- Higher viscosity than liquid metals

  - o Less entrapped gasses

  - o Less oxides; more machinability

  - o Better surface finish

  - o Can be easily automated

- Lower flow stress than solid metals

  - o Lower cost part forming

- Ability to incorporate other metals

  - o Composites

2.2.4 Swirled Equilibrium Enthalpy Device (SEED) technology

It is a method based on the "Rheocasting" technique for producing the Aluminum semi-solid dough. It should achieve a rapid controlled thermal equilibrium between molten Aluminum and metallic crucible. The controlling elements are in this case pouring temperature and stirring duration. The steps for the SEED technique shown in Figure 2.6 which begins by pouring the semi-solid paste, then, swirling with controlled temperature and duration. Following that, drainage of excess liquid, de-moulding and transfer to press and finally high pressure die casting (HPDC) to the final shape [19]. It is very important to maintain

temperature of the metal dough in the exact required temperature to avoid partial solidification before HPDC. This is accomplished by using special sophisticated machinery that maintains thermal equilibrium between the crucible and the metallic dough during the whole process of swirling [27–29].
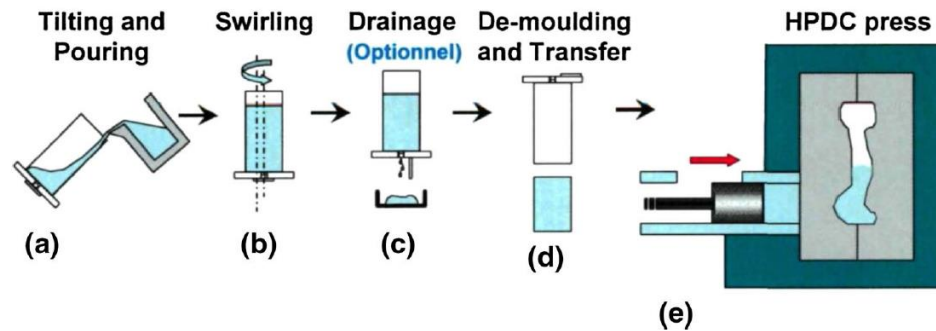
Figure 2.6:   Schematic diagram of SEED technique (a-c) and HDPC (d-e) [8].

2.3 Effect of multiple thermal aging on the mechanical and microstructure characteristics of A357.0

As mentioned above, the as-cast A357.0 is characterized by the presences of Mg and Si segregation in the Al matrix. The widely used heat treatment process for this alloy is the T6 thermal treatment, in which solution heat treatment helps in dissolving them back to the matrix [30]. However, recent studies have proven the superior mechanical properties that can be obtained by using multi-step thermal aging rather than T6. The results of the tensile testing done by H.Zhy et al [31] shown in Figure 2.7. Samples were solution heat treated at 543 °C for 12hrs then quenched in water maintained at 80 °C. Single stage aging was done at temperatures 155, 165 and 175 °C for 4h to 16h. For step aging, samples were pre-aged at 155 °C for 4h then finally aged at 175 °C for 3h to 18h.

The results show enhancement in the strength and ductility values of samples that were step aged for 12h as shown in Figure 2.7a. It is also observed general enhancement in the tensile properties of the step aged samples on the single aged samples.

The explanation of the high strength and ductility is the presence of different precipitate sizes of Mg_2Si. Figure 2.8a shows the TEM imaging of A357 semisolid cut from the control arm and aged according to the multiple interrupted WC3 (Figure 3.2). It is observed the different sizes of Mg_2Si that compromise between strength and ductility. In the contrary of Figure 2.8b that is of nearly similar alloy and shows same precipitates size under single aging condition.
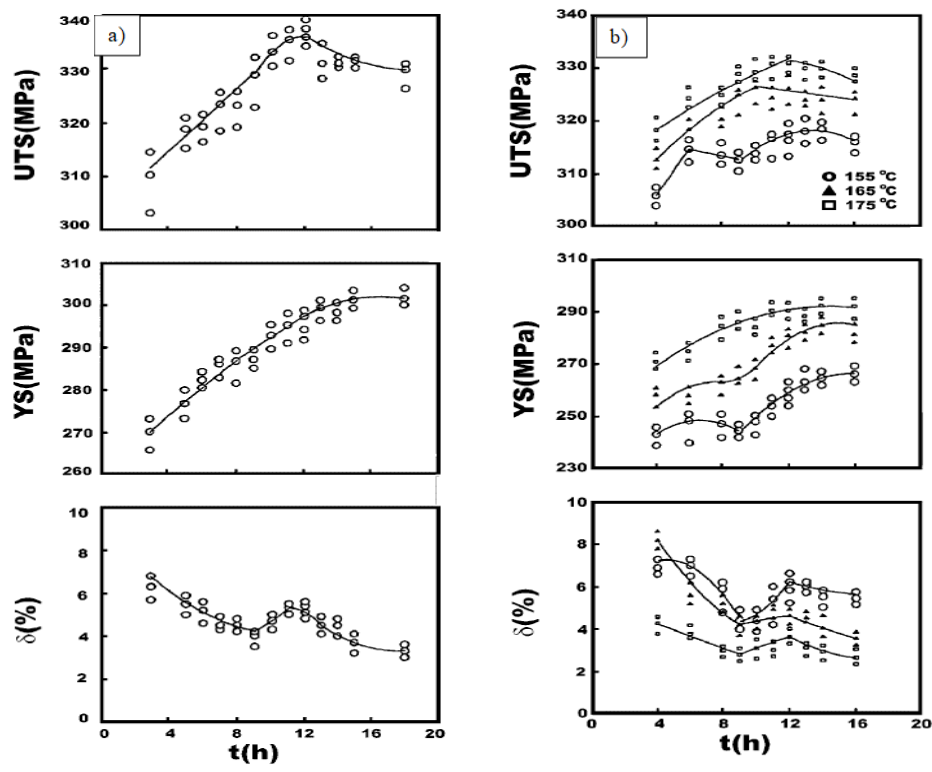
Figure 2.7:   Mechanical properties of A357 alloy a) two-stage aging, b) single-stage aging [31].
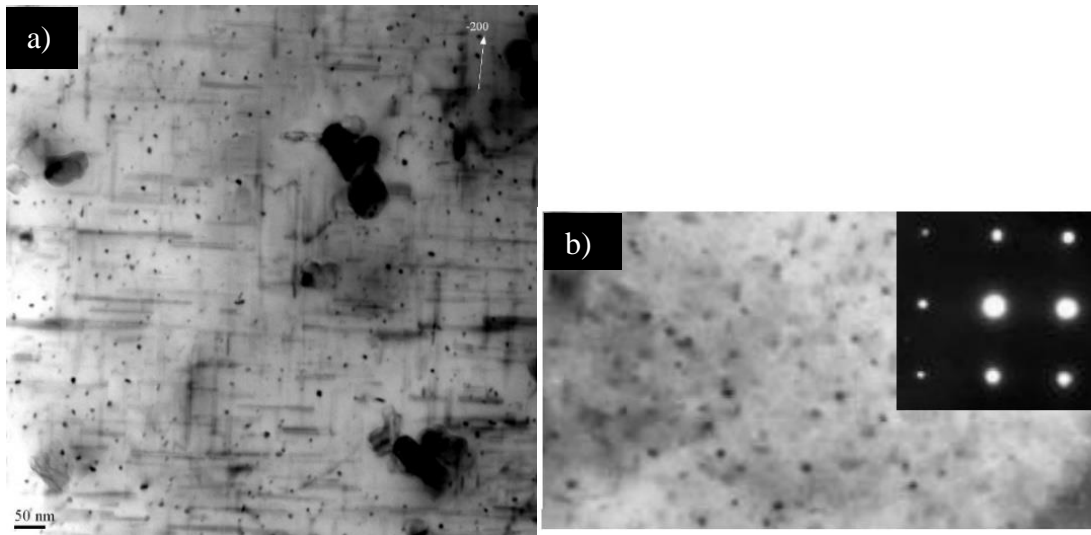
Figure 2.8:   TEM imaging showing Mg2Si precipitates (a)A357.0 multiple aged (WC3), (b) Al-0.65Mg-0.7Si aged at 175 °C for 30 mins.

Table 2.3 shows the measures of the different sizes of Mg_2Si for several different aging cycles (shown in Figure 3.2). The values show large differences in sizes as a result of the multiple aging.

Table 2.3:   Average length of Mg_2Si precipitates of A357 multiple aged [32].

Thermal Aging Cycles	Average Length, nm	
WB$_5$ (T7/T6)	10.5 ± 1.4 nm	46.27 ± 0.6 nm
	82.42 ± 1.7 nm	199.12 ± 1.2 nm
WB$_8$ (T7/T6)	28.1 ± 2.3 nm	56.7 ± 1.1 nm
	98.47 ± 1.8 nm	245.21 ± 2.1 nm
WC$_3$ (T6/T4/T7)	10.32 ± 1.4 nm	32 ± 1.1 nm
	80.5 ± 2.1 nm	206.47 ± 1.9 nm

Since the aluminum A357 is the material used in manufacturing of the suspension lower control arm in this study; the design of such component also has a great role in its fatigue life. It is important to gather information about new trends in suspension systems in general, as well as, the optimized -or recommended- designs of various types of control arms.

The next subsection focuses on researches done automotive suspension especially the McPherson strut suspension. Also, a collection of different studies applied on various types and designs of control arm is found. The sub-section ends by the latest study and recommendations for the control of interest in this project done by the same group (Laboratoire de modélisation en mécanique des solides appliquée (LM^{2}SA).

2.4   Lower control arm design development

The development of vehicle suspension components especially lower control arm has always been the matter of research in recent studies. Lower control arm is the major component in the MacPherson strut suspension. A complete understanding of this suspension system is thus required in order to understand the type of forces to expect and the direction of these forces.

2.4.1   MacPherson strut suspension system design review

The control arm in vehicle suspension is connected to the chassis by means of a rotational joint in the form of a simple hinge. The lower control arm from the other end is connected to the vehicle hub by means of a ball joint. A tie rod is responsible for the steering action and is also connected to the wheel hub with a ball joint. MacPherson suspension system supports the weight of the vehicle by means of this wheel hub with the interference of the control arm. However, the control arm is only responsible of maintaining the kinematic location of the wheel and supporting transverse loading as acceleration and braking [33]. MacPherson strut suspension is favorable over the double wishbone (DW) suspension system for commercial city vehicles. It is characterized by its simple design, consuming much less space; thus,

saving weight and allowing more room for the front drive axle. The MacPherson suspension is also relatively inexpensive compared to other suspension systems. One of the biggest advantages of this suspension system is the decreased unsprung mass[2] which has a direct effect on vehicle performance and comfort. However, the main disadvantage of this suspension system is that it cannot allow vertical movement without the changing of the camber angle of the wheel. This can cause instability especially in off-road conditions; consequently, DW mechanism is used in off-road cars [34].

2.4.2 Effective forces on lower control arm

Forces acting on vehicle tires can be calculated in the three dimensions x, y and z; such that the x-component is the longitudinal force ($F_{Long.}$), y-component is the lateral force ($F_{Lat.}$) and z-component is the vertical force (F_V) as shown in Figure 2.9. While the vertical force is due to the vehicle weight, and lateral force is due to camber and toe angles; the force of importance in this project is the longitudinal force [35]. The longitudinal force is the one supported by the lower control arm in the MacPherson suspension system. It is induced as a result of the rolling resistance force, as well as, traction or braking. Longitudinal force can be calculated by the combination of the rolling resistance force and the traction force. Rolling resistance force can be calculated by multiplying the coefficient of rolling friction 'f' with

---

[2] Unsprung mass is the sum of masses of all suspension components. It is crucial in the vehicle vibration response and plays an important role in the comfort of the sprung mass (vehicle body including passengers).

vehicle vertical load. While traction force can be calculated by multiplying the instantaneous value of the coefficient of friction $'\mu'$ with the vertical load. The equation can be written as:

$$F_{long.} = (\mu - f) * F_v$$
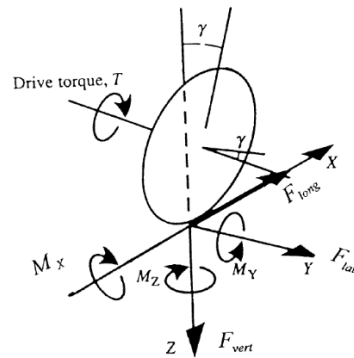
Figure 2.9:　　Forces acting on vehicle tire due to engine torque [36].

S.Hegazy etal [36] has created a model of a moving vehicle performing the maneuver shown in Figure 2.10 and calculating forces on wheel hub using ADAMS (automatic dynamic analysis of mechanical systems) software.
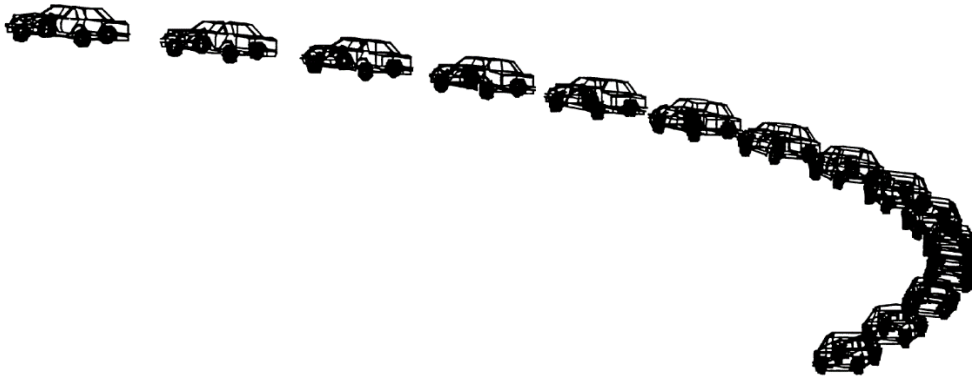
Figure 2.10:　　Simulated vehicle maneuver for 5s [36].

The mass of the vehicle body used was 1185 kg which is a very good value for representing modern commercial vehicles. The results for the longitudinal force was calculated and plotted in Figure 2.11. The value of the maximum force due to a bump stop on the front tires is around 1800 N. This value multiplied by a suitable safety factor can be used as a clear guide of the amount of force the control arm should be able to support.
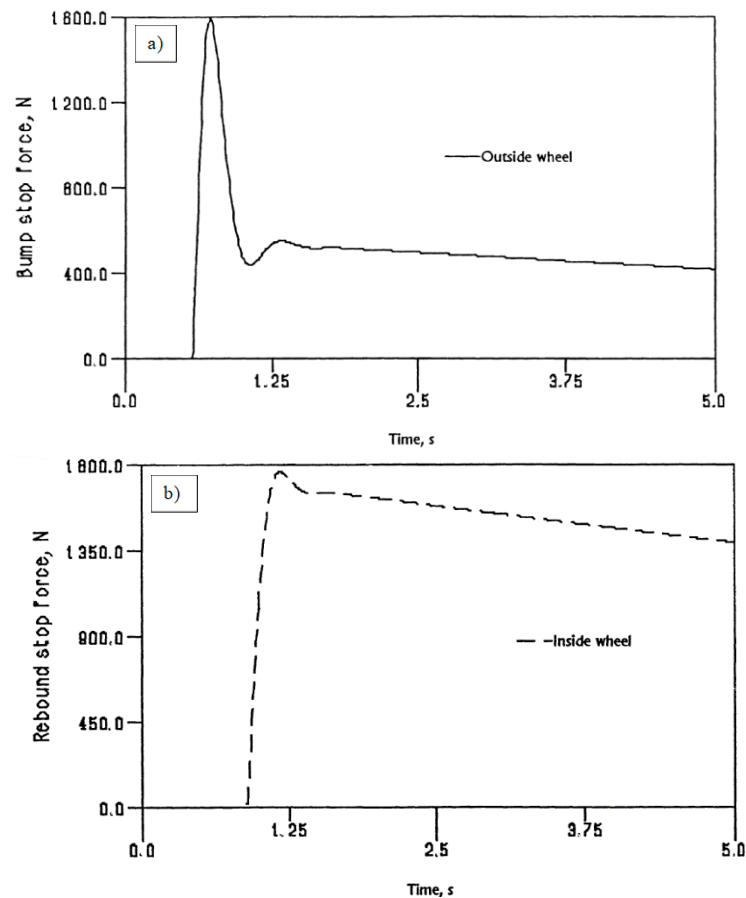
Figure 2.11:   Results of ADAMS simulation (a) Bump stop forces for front tires and (b) rebound stop forces for front tires [36].

A simulation done by X. Ning etal [37] was done to optimize the ride comfort requirements using ADAMS software. The study used the values of 4~12.5 Hz as the most sensitive

frequency range of driver seat vertical axis weighting frequency. And a value of 0.5~2Hz for horizontal frequency [38].

2.4.3   Structural design of control arm

Control arm has many shapes all is expected to possess an advantage over the other design. The understanding of the different approaches in the production of the optimum or best design is important in the design part in this project.

An optimization study was carried out by M.Viqaruddin and D.Reddy [39] using Radioss software. The control arm (shown in Figure 2.12) used in this study was of the wishbone type. The 3D model was created using the CAD (computer aided design) software, CATIA V5. The part was meshed using HyperMesh by using 10 nodes tetrahedral elements with topology optimization. Spider webs where used in each loading slot to better represent load action.
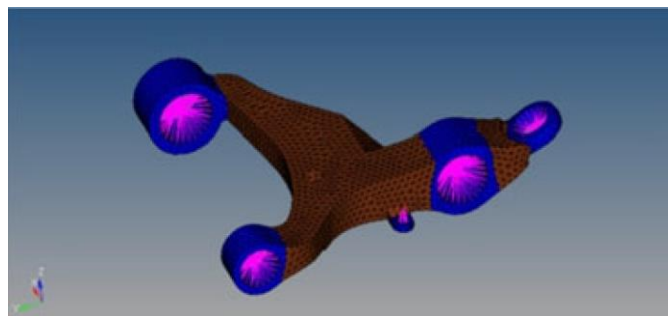
Figure 2.12:   Original wishbone control arm used in optimization study with meshing and 'spiderweb' shown [39].

The optimization tool solves for stress values, given factor of safety and displacement as constraints. The objective function is to minimize the weight and material used of this part. The optimized design of the wishbone shown in Figure 2.13 shows a 30% weight reduction

than the original design. A number of ribs can be observed, which has replaced the solid

middle web of the original design. These ribs can give the structure its needed strength while

minimizing the weight as much as possible.

Figure 2.13:   Optimized design of the wishbone control arm [39].

The work of A.Bouaicha [40] has proposed three different design of lower control arm

seeking to enhance stress distribution and weight of this part. The different designs are shown

in Figure 2.14 in which the mass of each is 1200 g, 12272g, 1227 g and 1212 g for designs

a, b, c and d respectively. It can be observed that the conventional design has a slightly less

weight than all other proposed designs.
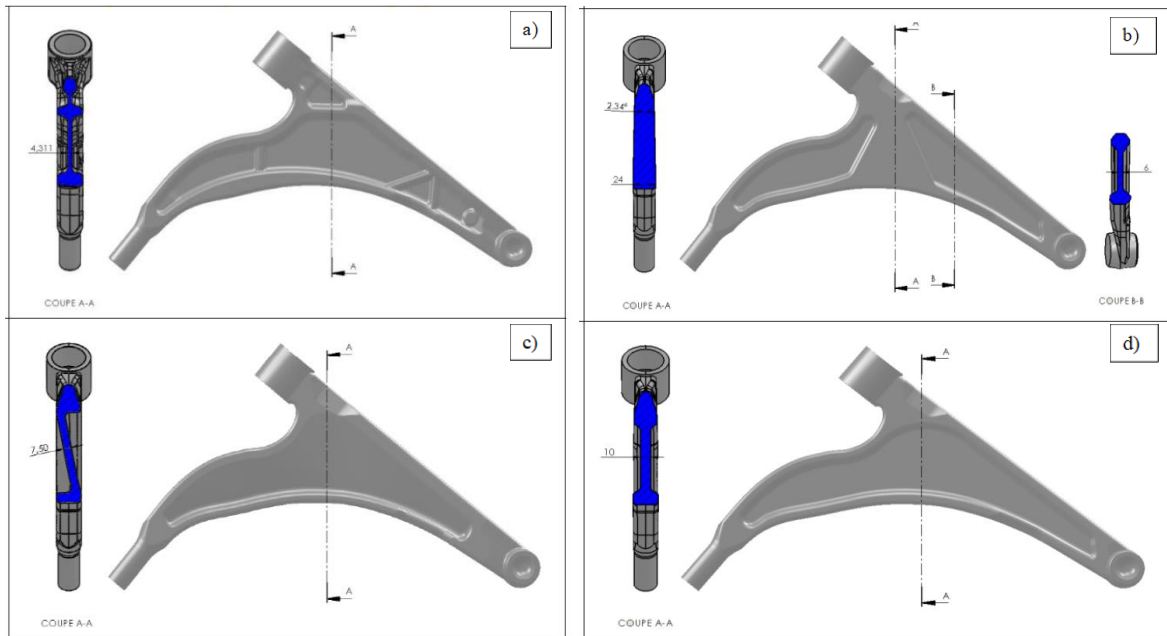
Figure 2.14:   Proposed designs of lower control arm. (a) Conventional design, (b) central thick web design, (c) Z-shaped design and (d) 10 mm central web design [40].

The Z-shaped design (Figure 2.14c) was recommended due to its good stress distribution as well as it superior castability compared to the conventional design. The inclined web in the Z-shaped design is believed to enhance stress distribution; thus, preventing stress raiser zones. The results of the Von-Mises stress distribution is shown in Figure 2.15, which shows a maximum value of 199 MPa when subjected to a 5.5 kN longitudinal force. It can be observed the high density of zero stress regions (blue regions) which indicate that this design can be even enhanced.
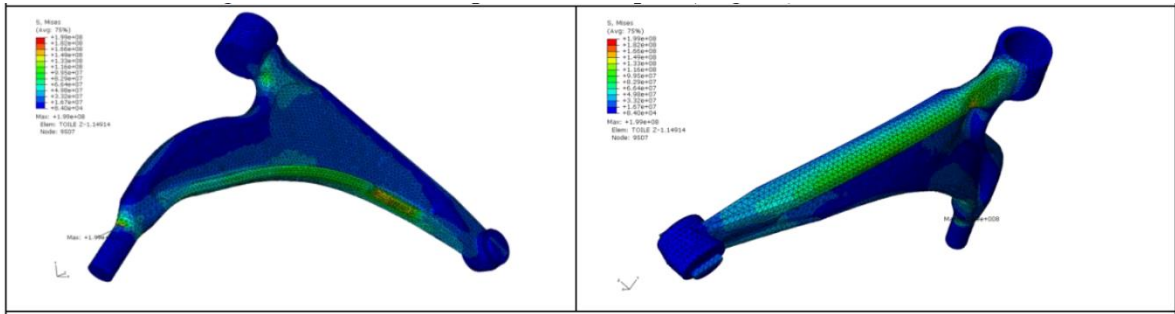
Figure 2.15:   Von-Mises stress distribution of Z-shaped design from literature [40].

The most significant enhancement of this Z-shaped modified design is its superior castability and being suitable for semi-solid casting technique. Figure 2.16 shows the results of ProCAST simulation using the fluid parameters of the A357 alloy in the semi-solid phase. The simulation shows a complete laminar flow of the semi-solid dough throughout the geometry of the control arm. It can also be observed the absence of any fluid plunging which may cause porosities and casting defects. The Z-shaped was therefore recommended due to its good stress distribution and superior castability.
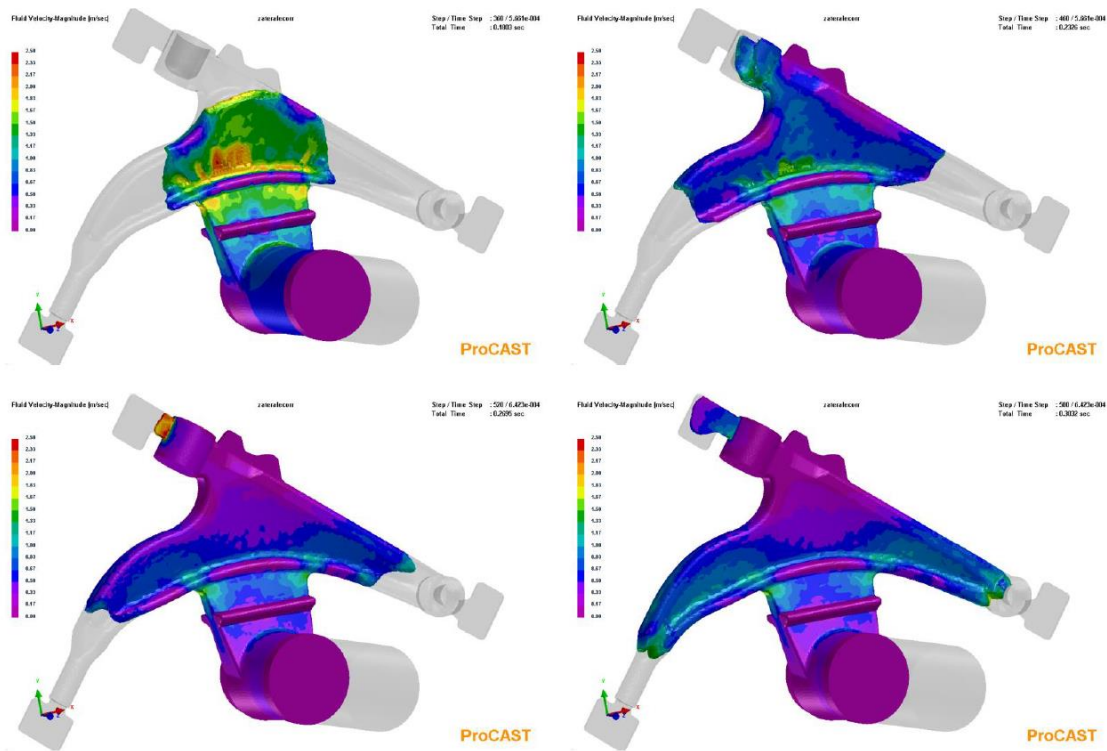
Figure 2.16:   ProCAST simulation of the Z-shaped design from literature [40].

As the design of the control arm has been reviewed, and previous design approaches have

been understood; causes of failure this part should be evaluated. It is important to know what

to predict as a type of failure of this component which will help the design approach.

2.4.4   Failure of lower control arm

Manufacturing of first generations of lower control arm employed nodular cast iron as its

material, and it was often used as cast without any thermal treatment [41]. Recently, control

arms have been manufactured from different steel grades using forging to reduce the part's

weight. The introduction of aluminum alloys in automotive industry to substitute steel has

shifted manufacturing techniques back to casting as it is more economical than forging. The

most common disadvantages of casting are inhomogeneous microstructure and uneven

mechanical properties. Furthermore, shrinkage during casting solidification can cause compressive residual stresses in the material of the control arm. The study of the effects of these defects is very important in the development of the design of this mechanical component.

Suspension control arms are subjected multiaxial fatigue with variable amplitudes due to the different road conditions. As a result, microstructure variations, casting defects, residual stresses and stress triaxiality should be integrated in the design of such components [42]. A study by Y.Nadot etal [42] on lower control arm fabricated form nodular cast iron of 95% ferrite and 5% pearlite was conducted to show the effect of casting defects, as well as, loading cycles on the total fatigue life. An experiment of the setup shown in Figure 2.17 was used with a frequency of 10 Hz for all real test samples. Loading condition of interest to compare with this project was set at 1573 daN (15.73 kN) in the positive x-direction with and R factor of -0.5.
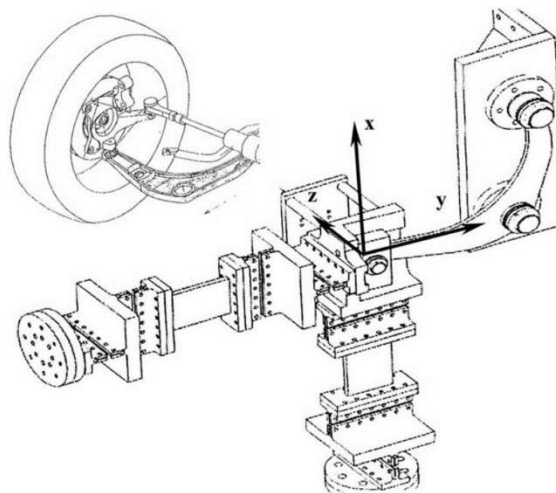
Figure 2.17:   Setup of fatigue testing for control arm of literature [42].

The results shown in Figure 2.18 represent the failure percentage of lower control arms in the load vs number of cycles curve. It can be observed that 90% of control arms have an infinite fatigue life at around 19 kN of maximum force for the cast iron control arm. The study also concluded that the most common reason of fatigue failure is resulted from oxides at the surface of the control arm [42].
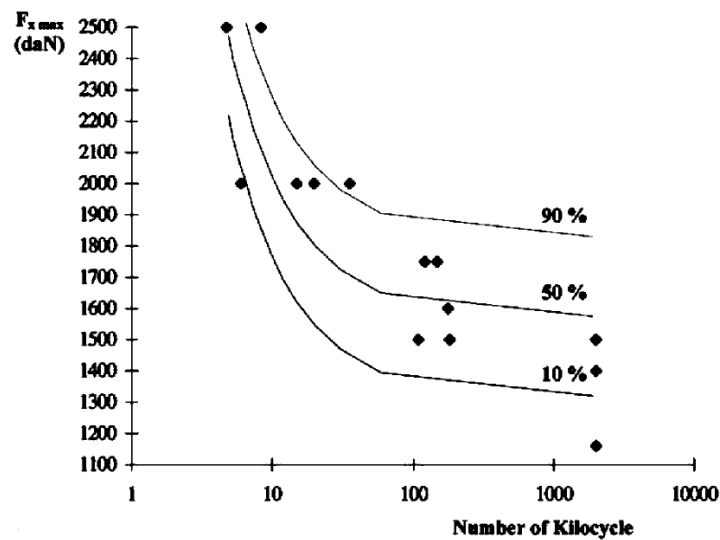
Figure 2.18:   Results of fatigue experiment in [42],plotting maximum force in dekanewtons vs number of cycles.

The fractured surface is shown in Figure 2.19 showing the surface casting defect causing failure. The SEM imaging of the fractured surface is shown in Figure 2.20, and it can be clearly observed the presence of internal shrinkage and oxides that was the main reason of failure.
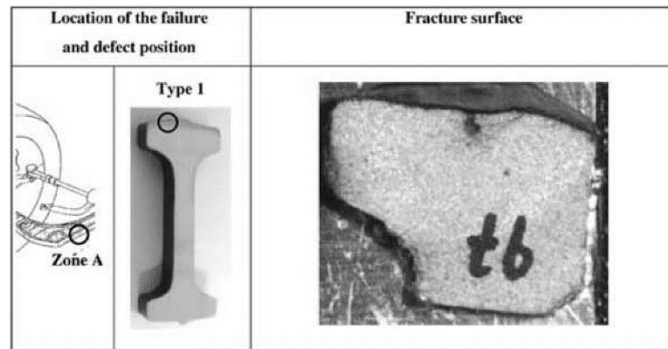
Figure 2.19:   Fracture surface of failed control arm showing the presence of oxides at the surface [42].
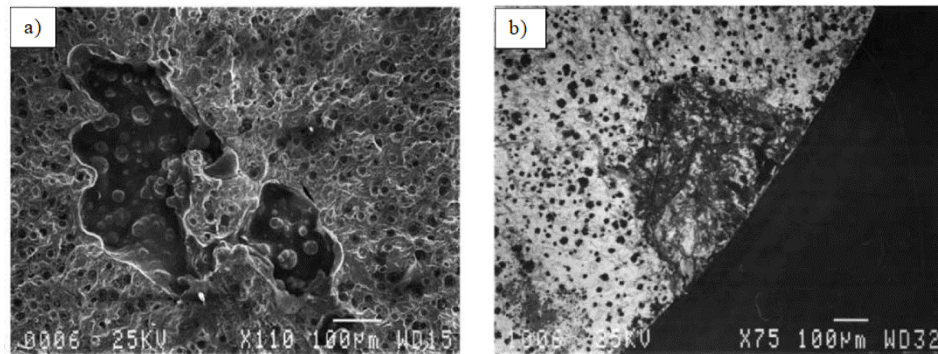
Figure 2.20:   SEM of fracture surface showing casting defects, (a) internal shrinkage and (b) oxides at surface [42].

From this study and others discussed in this sub-section, it can be concluded that the design of lower control arm can be optimized regarding its geometry. It is also very important to integrate casting defects and the effect of multiaxial fatigue in the design of such component. The combination of all these factors can lead to a superior control arm in terms of total fatigue life.

Chapter III

Materials & Design

3. Materials & Design

The plan of experimental work is based on performing different thermal aging cycles on either the applicable part or standard test samples. The heat-treated parts and samples are then proceeded to be tested using the adequate experimental settings. The heat treatments which are carried on tensile samples are evaluated used in the decision of the following test. The methodology begins with explanation of the heat treatments performed on different test samples. Then, each experimental test is explained in details, and at the end, the explanation of the finite elements configuration used is found.

3.1 Heat treatment

The results found by Elgallad,E.M et al [43], Ragab K. et al [44] and AbdulWahab M. et al [45] shows enhanced mechanical properties of the alloy under multiple thermal aging. As a result, a total of 13 different aging cycles is proposed according to the best results found by the literature as follows:

A. T6/T7 double step aging condition.

B. T7/T6 double step aging condition.

C. T4/T6/T7 multiple interrupted aging condition.

The oven used for all thermal treatments was the Pyradia Belfab (Figure 3.1) HM 1200 that operates at 600 volts 60 Hz with a 3-phase power supply. The oven can operate till a temperature of 600 °C which is enough for all aluminum thermal treatments. Figure 3.2 shows the different aging cycles A, B and C as well as the two-stage solution heat treatments.

Figure 3.1:   Pyradia Belfab thermal treatment oven.
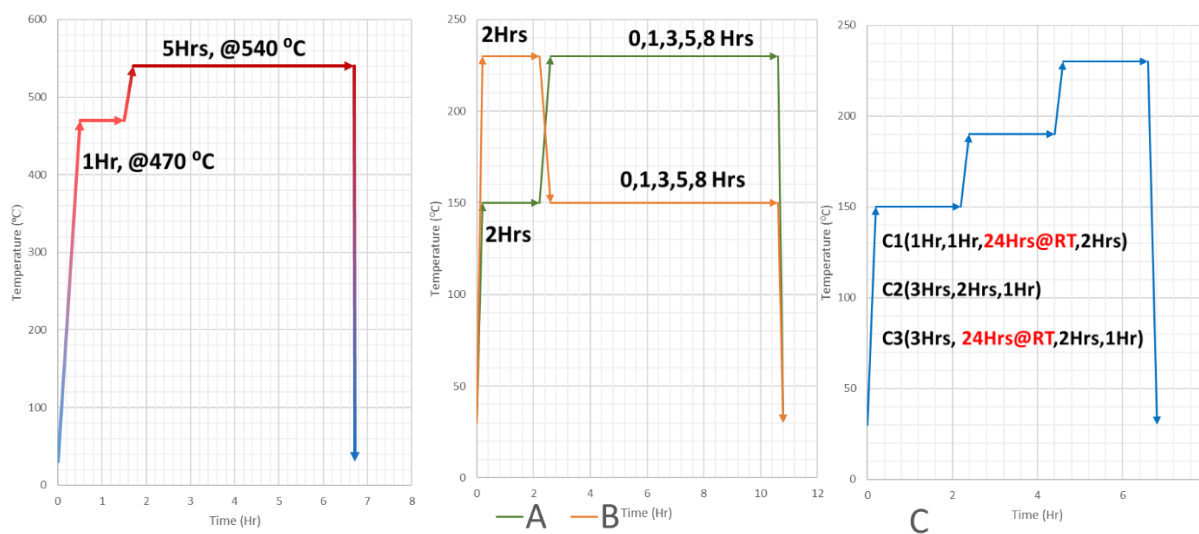
Figure 3.2:   Heat treatment illustration curves.

Solution heat treatment was carried out in two steps; at 470 °C first for 1 hour in order to

dissolve the $Mg_2 Si$ precipitates in the aluminum matrix. The heating rate was set to be around

5.89 °C/min or to rise from room temperature to 470 °C in 75 mins. This heating rate was

set after observing the maximum power and the overshoot of the furnace. It is very important to set an adequate heating rate in order to prevent high temperature overshoot but also insure that the process takes the minimum time to decrease overall cost. The furnace was then set to rise to 540 °C in 30 minutes after that to dissolve iron intermetallics as well as the remaining Mg and Si. Samples were then quenched in water maintained at a temperature of 60 °C by means of an electric heater regulating the temperature of the quenching medium as shown in Figure 3.3. Samples were then left to natural age for 24 hours at room temperature before proceeding to the thermal aging heat treatments.

For the T6 standard heat treatment solution heat treatment was carried on at 540 °C for 8 hrs followed by artificial aging at 175 °C for 6 hrs according to the ASM handbook volume 4 [2] for the alloy A357.0.

Figure 3.3:   Quenching medium maintained at 60 °C by means of electric heater.

Internal temperature of the oven was monitored using a thermocouple to insure proper heat treatment temperatures. Thermocouples were attached to an aluminum piece of similar dimensions as the samples being heat treated. The values were then saved and revised after each heat treatment to ensure that the programming of the furnace followed the required plan described in Figure 3.2. The figures below show some of the curves generated by the thermocouple for the solution heat treatment as well as some of the aging cycles.
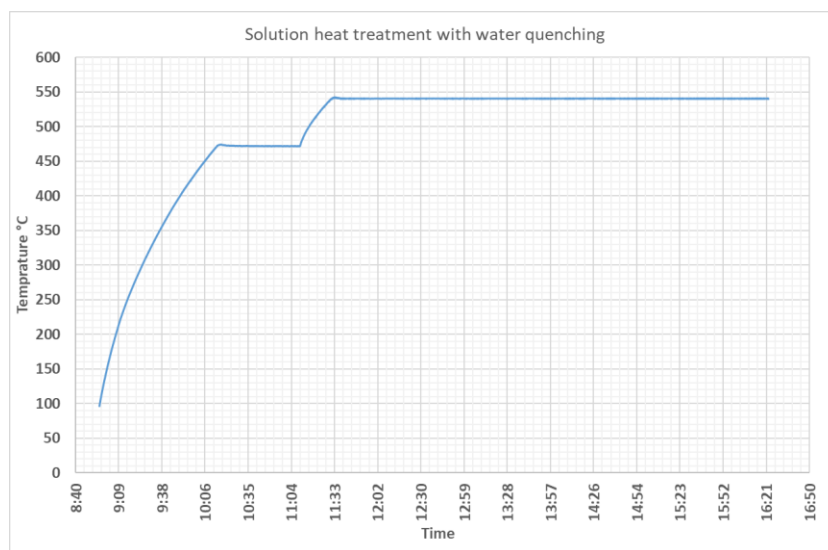
Figure 3.4:   Thermocouple curve of solution heat treatment.
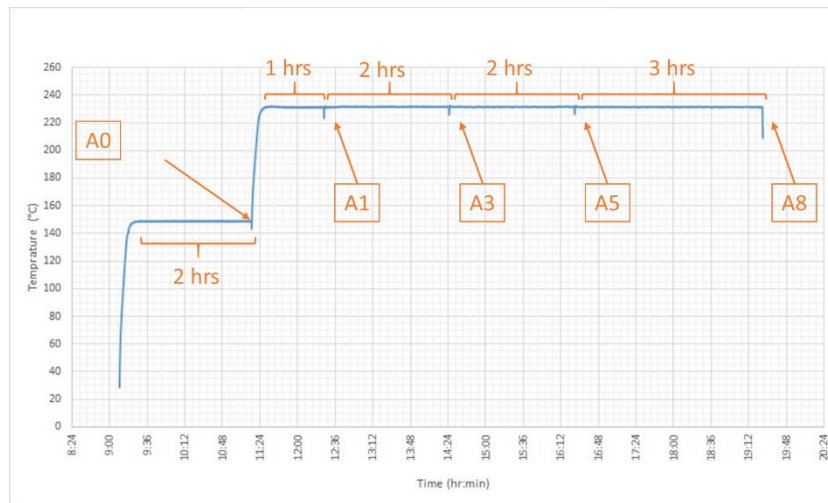
Figure 3.5:   Thermocouple curve of T6/T7 ("A" cycles) aging treatment.

It is observed in Figure 3.5 the sudden drop of temperature as samples were taken out of the oven every one to three hours. However, the drop is one around 5 °C as the samples were taken out quickly so that the heat drop doesn't affect other samples. The margin of 5 °C is considered to be acceptable for an operating temperature of 230 °C. In Figure 3.6 the heat drop is observed too but with a value lower than 2 °C for operating temperature of 150 °C.
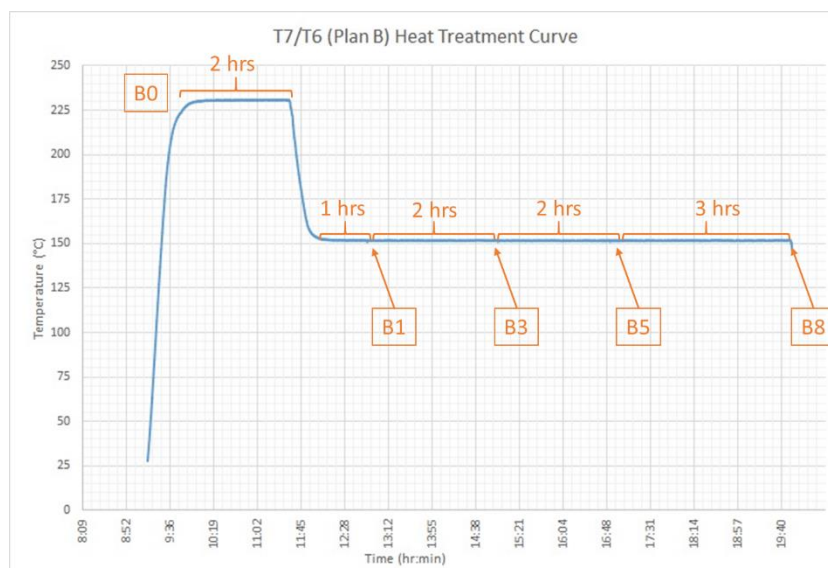
Figure 3.6:   Thermocouple curve of T7/T6 ("B" cycles) aging treatment.
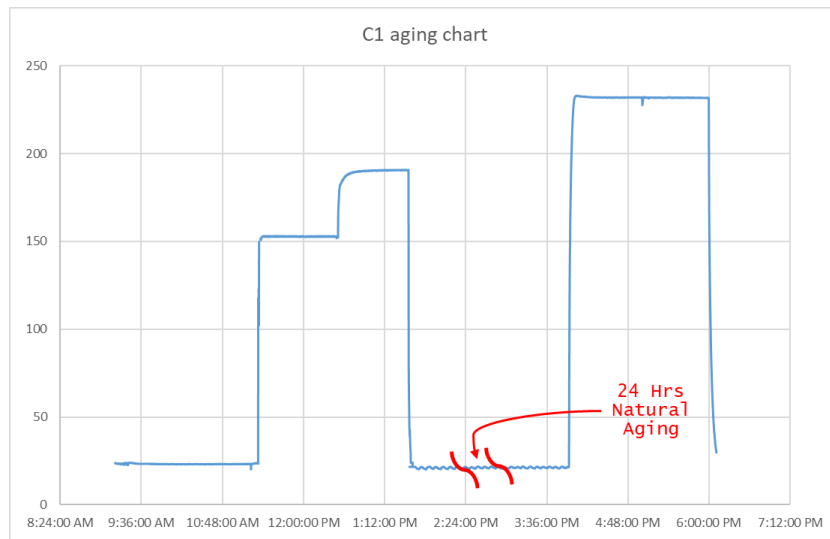
Figure 3.7:   Thermocouple curve of C1 aging cycle.
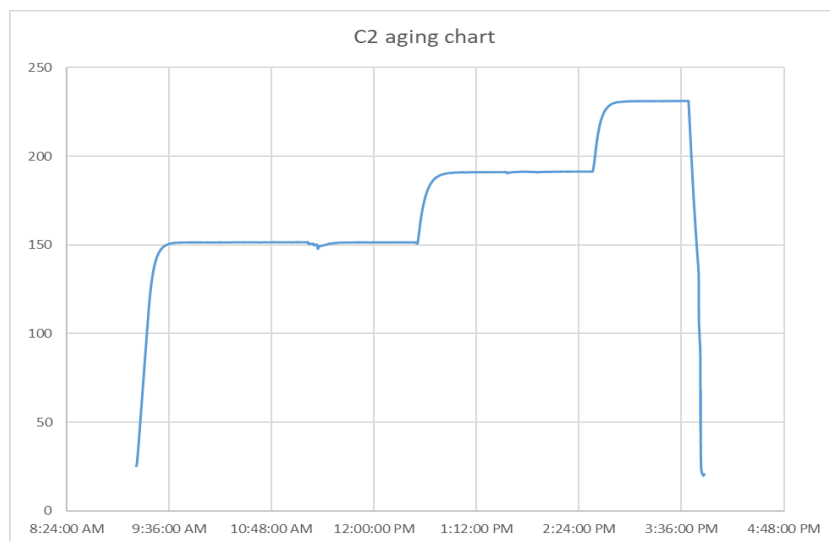
Figure 3.8:   Thermocouple curve of C2 aging cycle.
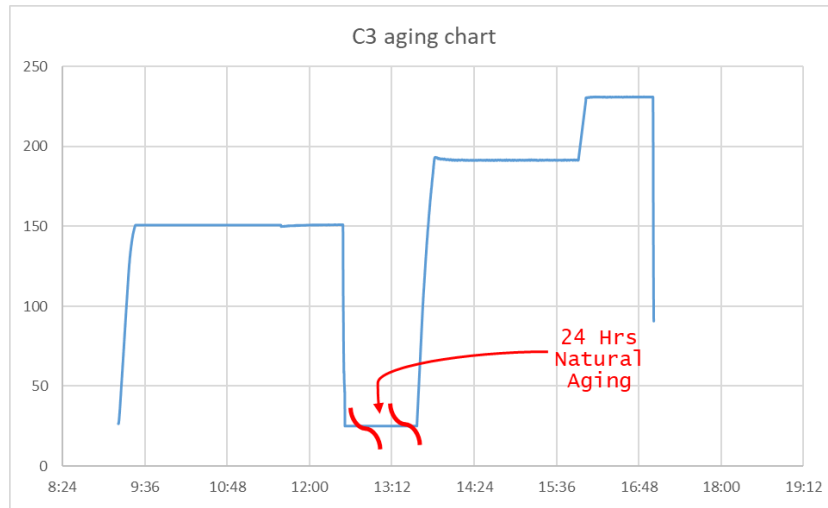
Figure 3.9:   Thermocouple curve of C3 aging cycle.

For Figure 3.7 and Figure 3.9 the aging cycle was applied on two consecutive days and their curves were combined in which the marked red area represents the 24 hours natural temperature aging. Times presented on each figure are real timing except for aging cycles C1 and C3 which can differ by around 2 hours as the curves were combined over two days.

3.2   Tensile testing

Tensile testing is important in determining the mechanical properties of the different aging cycles. It is a very well-known testing method that has been used since long time. The results of tensile testing are reliable, and it is the best method of determining some important mechanical properties as the yield strength, the ultimate strength and the ductility or elongation. As the goal of this experimental work is to select the best aging cycle regarding fatigue life; tensile testing was the first approach in the methodology of this project. It helped to give a clear image of the quality of each aging cycle. Aging cycles that showed superior properties regarding YS, UTS and %E from the tensile testing are the ones that continued to
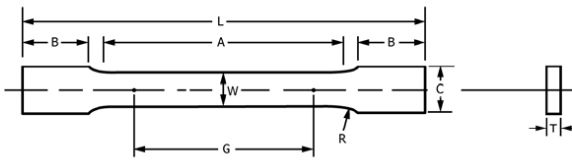
other experimental testing. On the other hand, aging cycles that showed inferior properties for both strength and elongation were excluded from other experimental testing. This step was very important due to the limited amount of A357 semi-solid samples, as well as, the limited number of real control arms. The following experimental work relied on the results obtained from the tensile testing in order to select the best aging cycles, and to either validate or contradict with its results. The experimental work was achieved in three steps: samples preparation, heat treatment and finally testing.

3.2.1   Sample preparation

Samples were prepared according to ASTM E8 standard as shown in Figure 3.10. The sub-size specimen (refer to Figure 3.10) was selected as it is the smallest specimen in the standard. It was also selected as the extensometer available has a gage length of 1 inch which is 25.4 mm which matches the standard only for the sub-size specimen. The standard allows a free choice of the thickness of the specimen so that it can be cut from any sheet metal thickness. As a result, the thickness selected in this project was 3 mm which was suitable to the thickness in which the material is available. Specimens were machined using a vertical milling machine and cooling was attained by means of emulsion during the machining process. Samples were then examined to have the same dimensions within the tolerance allowed by the standard. All samples were then cleaned using alcohol and any hard edges - if presented- that may affect the test results were sanded. Samples then proceeded to the next step which is the heat treatment.

ASTM E8/E8M – 15a

Dimensions			
	Standard Specimens		Subsize Specimen
	Plate-Type, 40 mm [1.500 in.] Wide	Sheet-Type, 12.5 mm [0.500 in.] Wide	6 mm [0.250 in.] Wide
	mm [in.]	mm [in.]	mm [in.]
G—Gauge length (Note 1 and Note 2)	200.0 ± 0.2 [8.00 ± 0.01]	50.0 ± 0.1 [2.000 ± 0.005]	25.0 ± 0.1 [1.000 ± 0.003]
W—Width (Note 3 and Note 4)	40.0 ± 2.0 [1.500 ± 0.125, -0.250]	12.5 ± 0.2 [0.500 ± 0.010]	6.0 ± 0.1 [0.250 ± 0.005]
T—Thickness (Note 5)		thickness of material	
R—Radius of fillet, min (Note 6)	25 [1]	12.5 [0.500]	6 [0.250]
L—Overall length, min (Note 2, Note 7, and Note 8)	450 [18]	200 [8]	100 [4]
A—Length of reduced section, min	225 [9]	57 [2.25]	32 [1.25]
B—Length of grip section, min (Note 9)	75 [3]	50 [2]	30 [1.25]
C—Width of grip section, approximate (Note 4 and Note 9)	50 [2]	20 [0.750]	10 [0.375]

Figure 3.10:   ASTM E8 standard of tensile samples.

Heat treatment of tensile samples was carried out as discussed in the heat treatment section. All samples were properly spaced and exposed to the same heating conditions inside the heat treatment oven. Thermocouples were attached to some of the test samples in order to insure the heating accuracy reaching the samples inside the oven. Samples that were solution heat treated and left for 24 hours at room temperature for natural aging were then left in a freezer at a temperature of around -18 °C to stop any further natural aging. This step was done as the aging cycles were not the same and that only one heat treatment oven was available. Three tensile samples were first tested for each aging cycle, then, two more samples were added to the conditions that needed verification. Figure 3.11 shows three tensile samples for each condition after heat treatment. Following the competition of the first round of samples heat treatment; specimens proceeded to the tensile testing.

Figure 3.11:   Samples after heat treatment.

3.2.2   Testing and tensile machine setup

The test was applied using the MTS Alliance RT/100 with a maximum capacity of 100 kN. Room temperature was maintained at around 22 °C during the whole testing. The experiment was set as shown in Figure 3.12 where each specimen was clamped at the two ends and an extensometer with 1 inch (25.4 mm) was used to measure the elongation[3]. Strain rate control was set for the machine during the test according to ASTM E-8. Strain rate was set to 0.5 mm/min which is around 0.019 mm/mm/min for the whole test as a constant speed. Determination of yield strength was set by the 0.2% offset method as it is the most suitable method for aluminum alloys. The maximum elongation was taken at the fracture point and was then verified using a digital Vernier caliper.

---

[3] Displacement of the cross-head is not preferred as the machine can be modeled as an elastic structure. Thus, cross-head measures the combined extension of the specimen as well as that of the machine columns.

Figure 3.12:   Set up of tensile test.

The gage length of 1inch (25.4 mm) was marked on all samples and was then used to measure the maximum elongation manually using a digital Vernier caliper to verify the test data. Experimental data was then evaluated and defected samples were marked and eliminated. The testing took place in two stages; in stage one three samples were taken for each aging cycle. After the comparison of data and eliminating defected samples; more samples were assigned for the aging cycles with defected samples. Figure 3.13 shows an example of a defected sample due to a casting defect, in this case the defect was very remarkable that failure was at the grips location. In other cases, defected samples were marked by fracture outside the gage length shown in the figure. One of the importance of marking the gage length before the beginning of the test is the identification of invalid test specimens.
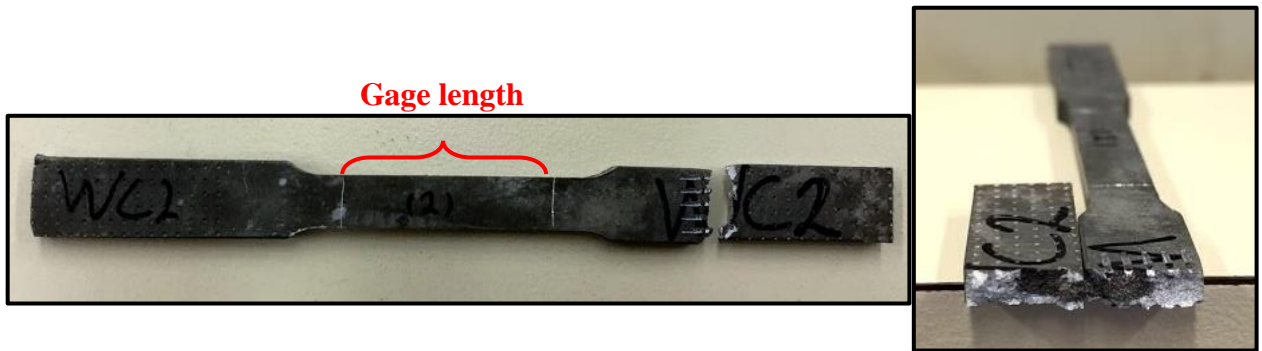
Figure 3.13:   Example of defected sample of tensile testing.

3.3   Lower control arm subjected to cyclic loading

The control arm fatigue testing is the best representation of control arm loading conditions in real life. The control arm is fixed to the testing machine the same way it is fixed in the vehicle and the load is applied to the location of the ball joint. The experimental work was divided into five phases; pre-testing and inspection, heat treatment, finite elements, testing and finally fracture analysis.

3.3.1   Pre-testing and inspection

Control arms were pre-tested before the application of heat treatment to insure that the part had no initial cracks. The control arm was loaded by a 2 mm amplitude sinusoidal cycle with a mean displacement of 0 mm. The 2 mm displacement corresponded to 7000 N of force on the tip of the control arm. Figure 3.14 shows an example of a pretesting curve for one of the used control arms. Each control arm was loaded by around 50 cycles in total, with a visual inspection of the part during loading cycles. The result of the pretesting was verified by the finite elements analysis using Ansys 19.1 static solver. The part was loaded by a 7000 N and the displacement was solved and found to be 1.7 mm as shown in Figure 3.16. The difference

between the 1.7 mm analytical displacement and the 2 mm experimental displacement is accepted as a machine error and/or combined deflection of the machine structure. As a result, all tested parts passed the pretesting inspection and continued to the next phase.
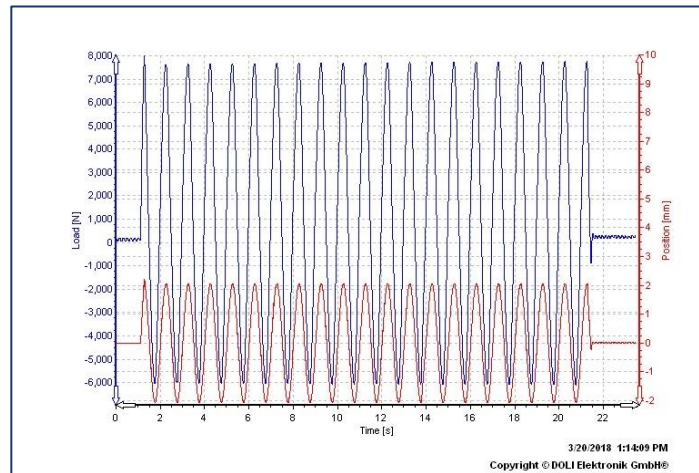
Figure 3.14:   Low cyclic fatigue pre-testing curve.

3.3.2   Heat treatment

Heat treatment was performed according to Figure 3.2 for selected aging cycles: WA0, WA1, WA8, WB0, WB5, WC1, WC3 and the standard T6[4]. Parts were quenched after solution heat treatment in water maintained at 60 ºC.

3.3.3   Finite elements simulation

Finite elements simulation was made before testing to predict reaction force and crack location. It is very important in determination whether the failure is a fatigue failure or a failure due to a defect. If the crack is observed in the critical zone shown in Figure 3.17 then

---

[4] Standard T6 for 357.0 alloy is 540 ºC for 8 hrs followed by 6 hrs at 175 ºC[2].

it is a fatigue failure and the part is not defected. Otherwise, if crack is observed elsewhere then there should be a defect that will be proven using SEM. The finite elements simulation was carried out using Ansys 19.1 according to Soderberg failure criterion (Figure 3.15).
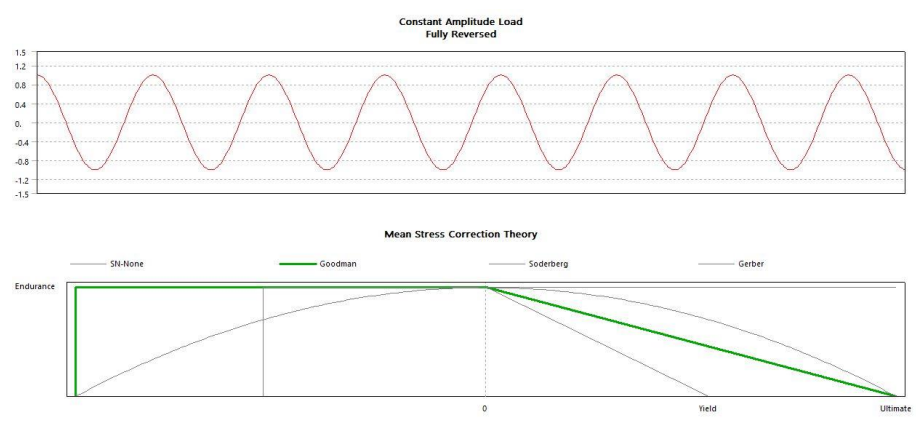
Figure 3.15: Illustration of loading condition and failure criterion.
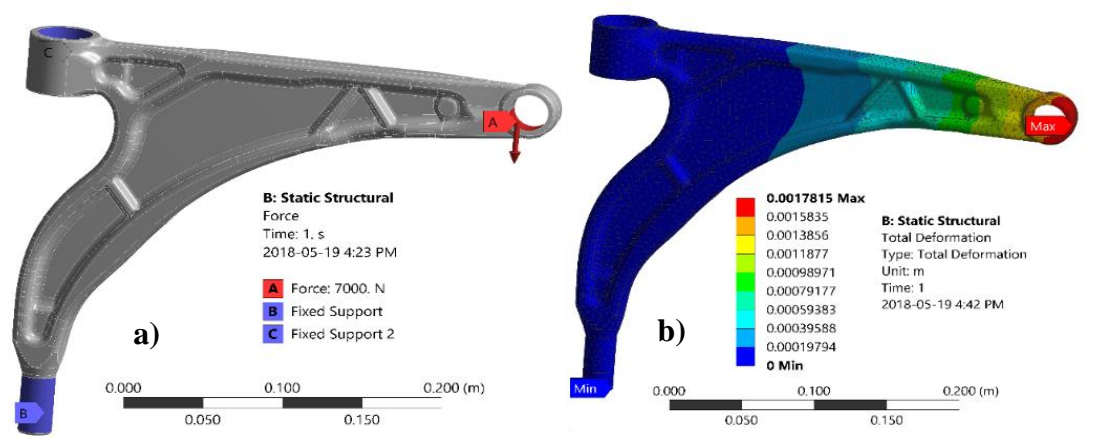
Figure 3.16: low cyclic fatigue FEA a) loading conditions, b) displacement plot.
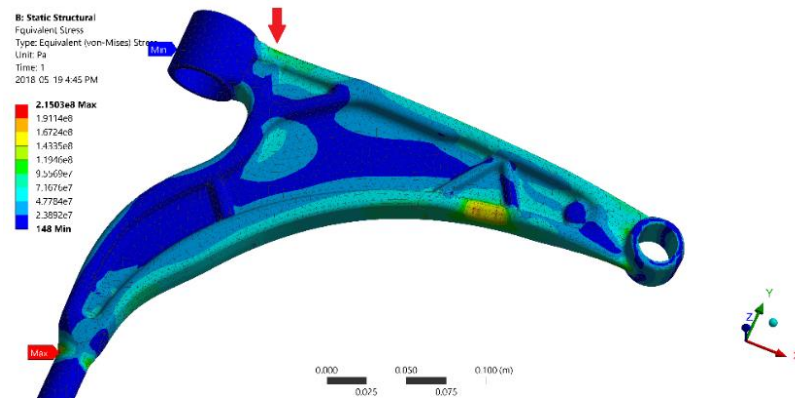
Figure 3.17:   Von-Mises stress of low cyclic fatigue FEA.

3.3.4   Testing

Control arms that have been pre-tested and heat treated were mounted on the hydraulic fatigue machine as shown in Figure 3.18. The machine exerts sinusoidal loading cycles of 7000 N amplitude and 1 Hz frequency until fracture of the part.
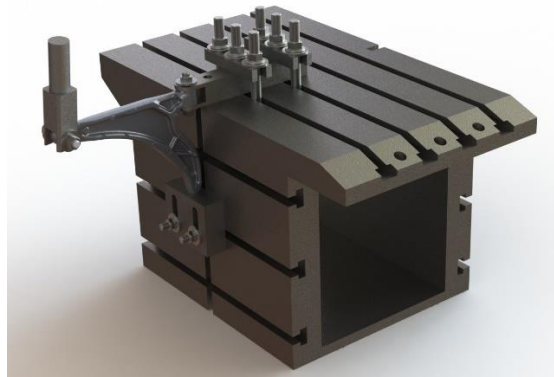
Figure 3.18:   Schematic control arm mounted on the hydraulic fatigue machine.

The fracture is observed as a discontinuity in the Load vs. Time plot as shown in Figure 3.19; and since the working frequency is 1 Hz, therefore the y-axis indicate the number of cycles

till failure. The failed specimen will only be accepted if the fracture is observed near the critical zone predicted by the finite elements simulation illustrated above.
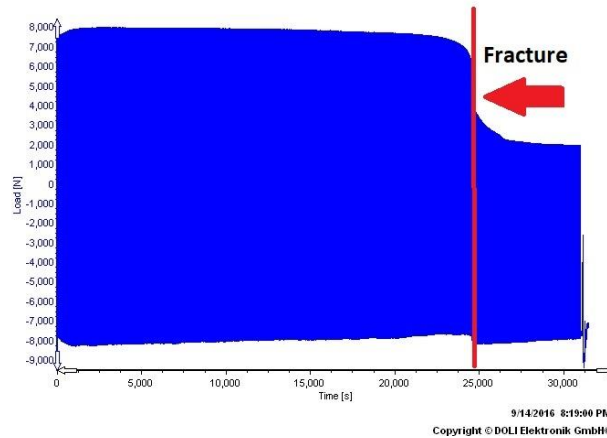
Figure 3.19:   WA8 Load(N) vs No. of cycles.

Examples of accepted parts are shown in Figure 3.20. Before the beginning of each test, parts were visually checked and any dark suspicious lines were marked. After test, if crack was found in the marked region part will be marked as defected and its result will be eliminated. The pre-testing inspection is very important as in the real part testing there is only one part per condition and the error should be minimized.
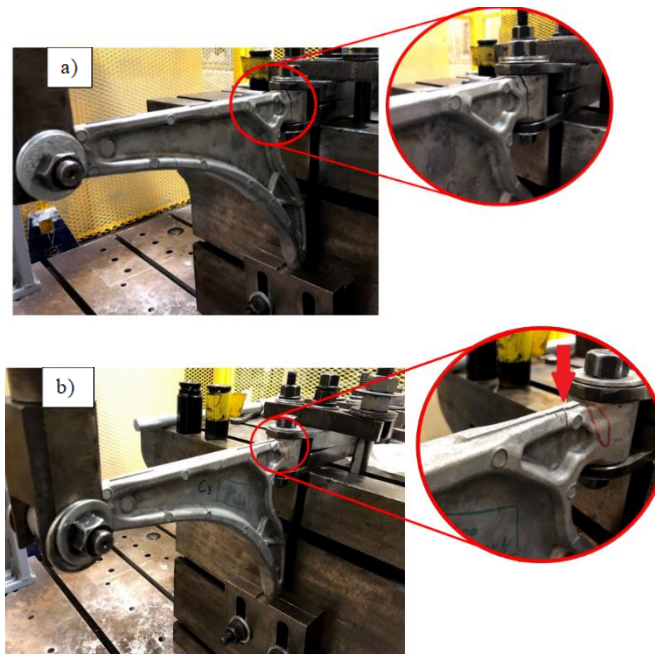
Figure 3.20:   Failure of fatigue samples a) WA0 b) WC3.

Figure 3.21 shows a defected sample in which the fracture occurred outside the expected zone by the FEA. Porosities and casting defects can be observed in the cross-section of the fractured sample shown in the figure below. Casting defects cannot be identified within the pre-testing phase due to the limited number of cycles in the pre-testing.
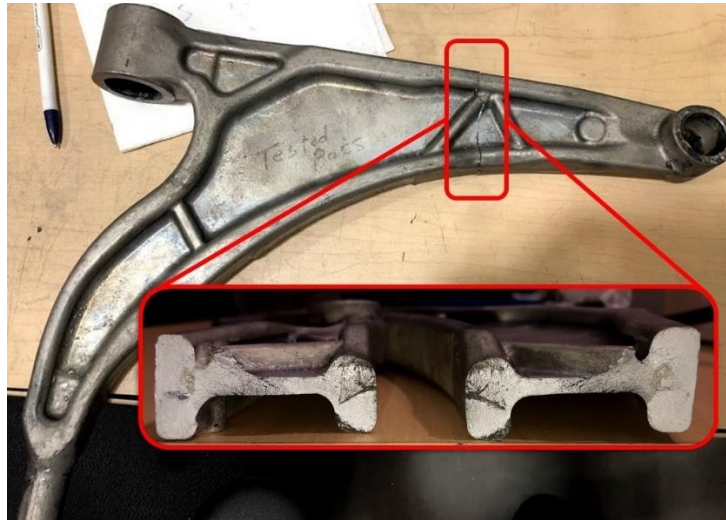
Figure 3.21:   Defected control arm sample fractured after testing.

3.3.5   Fracture surface analysis

Scanning electron microscopy (SEM) (Figure 3.22) was used to verify the microstructure characteristics concerning the type of fracture, and to detect cracks and defects (if present). This step is important to validate the fatigue results and to verify the cause of failure. The scanning electron microscope used is the JEOL JSM-6480LV with an accelerating voltage of 20 kV. The spot size was maintained at 45 nm for all samples, while the working distance ranged from 9 to 12 mm.

Fractured control arms were cut into small samples, one centimetre away from fracture surface, using and electric band saw operating at low speed. No emulsion or oils were used in the cutting process to prevent contamination of the fractured surface. Prepared samples were then mounted inside the SEM to be examined for the type of failure and the presence of defects. The images of each condition are discussed in detail in the next chapter.

Figure 3.22:   Scanning electron microscope used in examining the fracture surface of
failed control arms.

3.4   Constant deflection cantilever bending fatigue testing

The constant deflection cantilever bending fatigue testing is one type of fatigue testing

methods used. It subjects the specimen to constant deflection for high number of cycles till

fracture. Specimens are mounted in a way that is completely restrained from one end while

the other end is attached to the machine rocker arm. The rocker arm is adjusted so that it

maintains a constant stroke throughout the whole experiment regardless of the load on the

specimen.

The machine used is basically a crank-slider mechanism in which the specimen is attached

to the slider part. Figure 3.23 shows a crank-slider mechanism representing the operating

mechanism of the testing machine. The specimen is mounted in the slider position 'S' while

the motor rotates the crank 'R' with a constant angular velocity 'ω'. The stroke length is of

importance in this machine as it is the deflection to be applied to the specimen. As it is shown

in Figure 3.23 the stroke length can be altered by changing either the length of the crank 'R'

or the rocker 'L'.
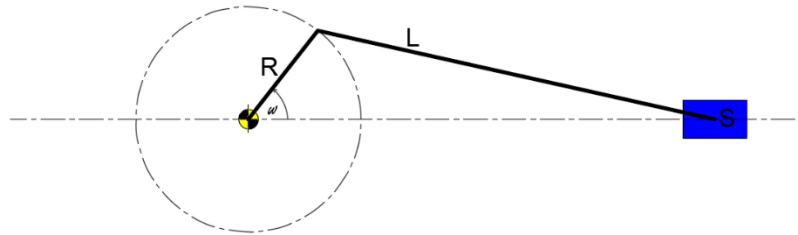
Figure 3.23:   Explanation of crank-slider mechanism of fatigue machine.

The fatigue test machine of interest uses an eccentric crank in which the eccentricity works

as the crank length; thus, changing the eccentricity of the device will change the stroke length

and the deflection applied to the test specimen. Figure 3.24 shows the eccentric crank in

which the stroke can be adjusted from 0 to 2.0 inches (50.8 mm). The eccentricity can be

changed by means of the five hexagonal bolts shown in the figure. The middle bolt is used

for the adjustment while the other four bolts are used to secure the crank in position so that

the stroke does not change during the experiment.
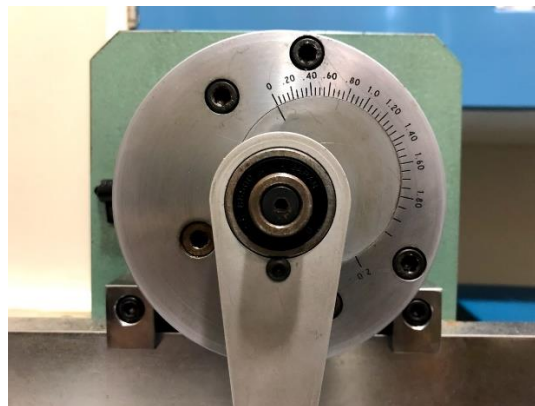
Figure 3.24:   Eccentric crank of fatigue test machine.

The cantilever fatigue bending testing is useful in determining the fatigue life of small fatigue samples in whic1h more than one sample for the same condition can be tested and compared to the results of the real part fatigue. It is also important in comparing other aging cycles of interest that were not tested as a real part.

3.4.1 Sample preparations

Samples were prepared as shown in Figure 3.25 [46]. Machined samples were grinded in order to remove machining scratches that will significantly affect the fatigue life of the specimen. The crack should lie within the narrow region in the middle; any fracture outside this region will mark a defected specimen. In order to remove the scratches resulted from machining; samples were grinded using sand papers from 120 to 600 grits. Figure 3.27 shows the scratches on the fatigue samples after machining and Figure 3.28 shows the effect of grinding on the surface of the sample.
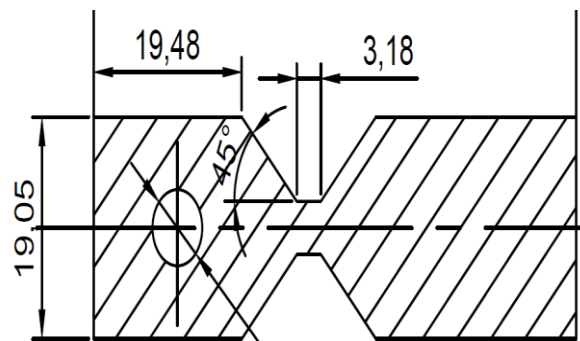
Figure 3.25:   High cyclic fatigue sample drawing (Dimensions in mm).

Samples were re-inspected after grinding using the steromacroscope shown in Figure 3.26 in which the images in Figure 3.27 and Figure 3.28 were taken.
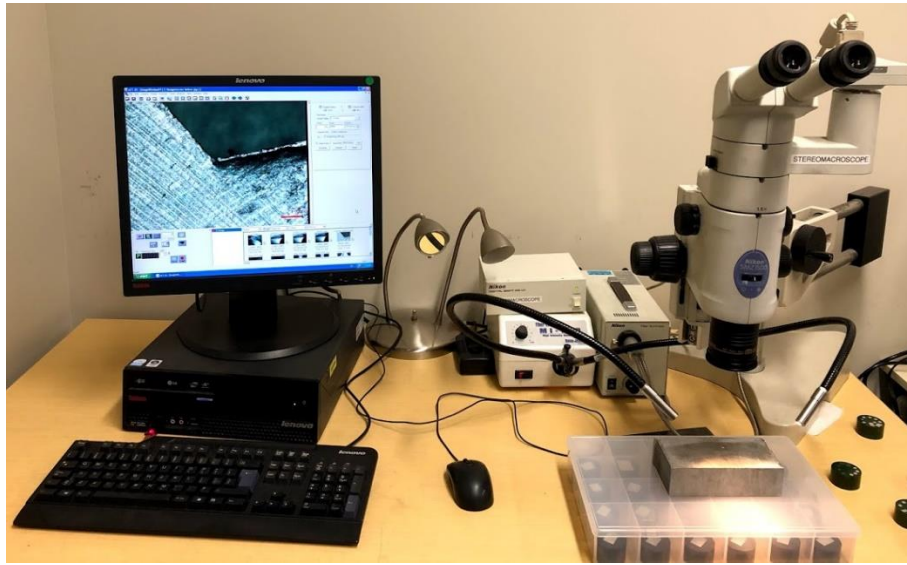
Figure 3.26:   Steromacroscope used in fatigue specimens surface checks.
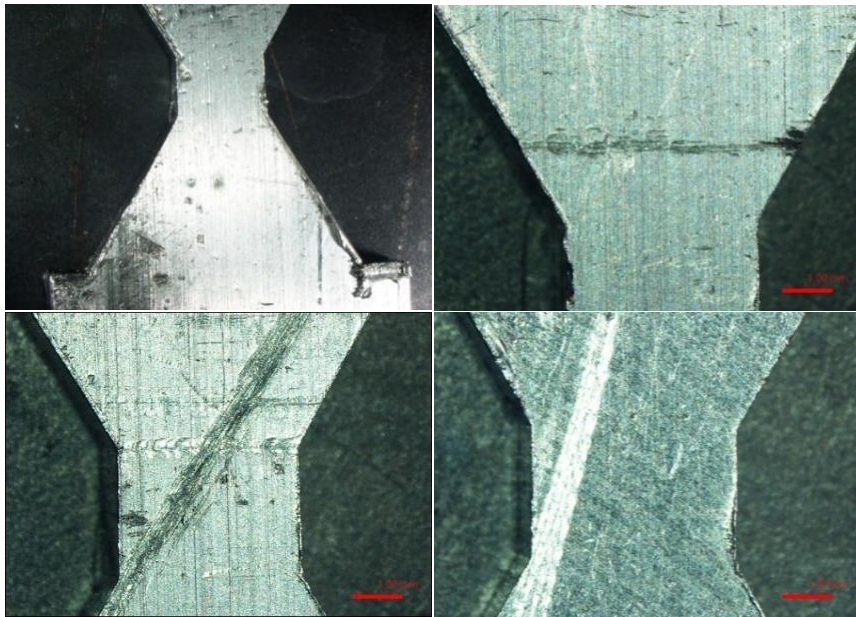
Figure 3.27:   Scratches on fatigue samples right after machining.
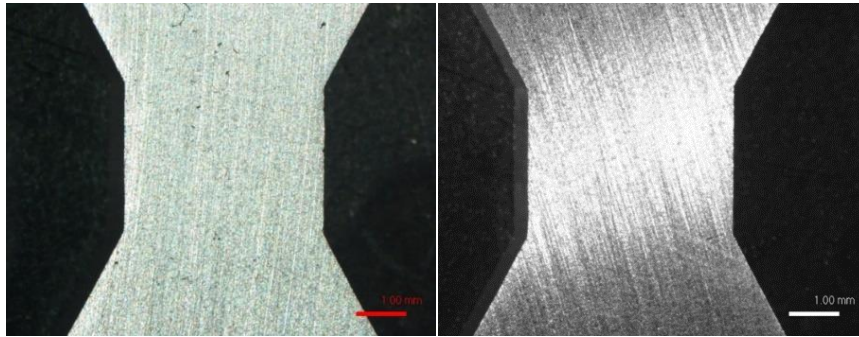
Figure 3.28:   Fatigue samples after grinding.

3.4.2   Heat treatment

Heat treatments illustrated by Figure 3.2 were applied on the mentioned fatigue samples. The following aging cycles were selected according to the results of both tensile and low cyclic fatigue: T6, WA0, WA1, WB0, WC1 and WC3. Before heat treatment samples were cleaned from any oils or grease contamination from machining. Clean samples were then equally separated inside the heat treatment oven for the solution heat treatment phase. Quenching was done by means of water maintained at 60°C as previous samples and then natural aged at room temperature of around 23°C for 24 h before proceeding the next aging phases. Other samples were stored in a freezer at a temperature of -18°C waiting for other aging cycles to be finished. Upon finishing from the heat treatment phase all samples were labelled by the name of their aging cycle and stored at room temperature to proceed to the next testing phase. 5 samples were taken for each aging cycle except WC3 had an additional sample for a sum of 6 samples for WC3. The total number of samples was 31 samples.

3.4.3 Testing

In this phase it was important to first calibrate the machine to ensure that all channels were working properly, and that the failure criterion was well defined for each channel. First, several dummy samples made from aluminum 6061 having the same exact dimensions complying to Figure 3.25 were tested. Samples first were used as taken from machining while others were grinded by the same way of the original samples and inspected using steromacroscope to compare the results of both cases. Figure 3.29 shows the results of both grinded and un-grinded test samples showing the effect of grinding on the values of the total fatigue life.
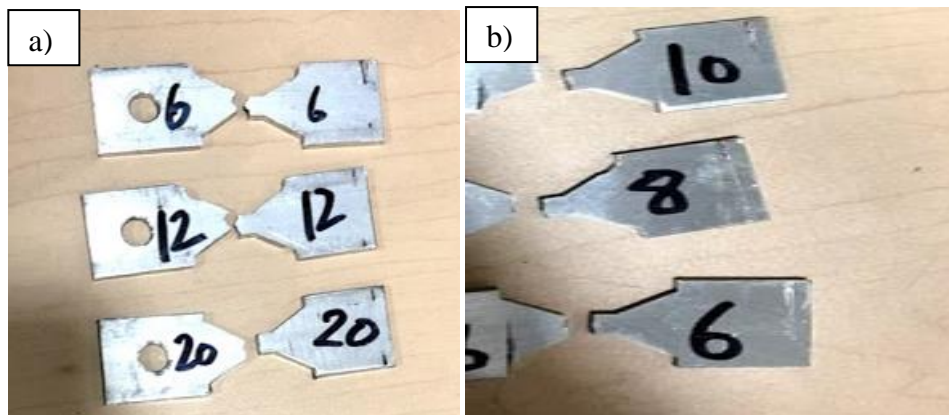
Figure 3.29:   Dummy samples for testing and calibration the fatigue machine. a) Before grinding, b) After grinding.

As shown in Figure 3.29 a, the values of the fatigue life are inconsistent with a large error due to the scratches presented already on the samples that act like initial cracks. While in Figure 3.29 b, the values are closer to each other with a relatively smaller error, as a result, all samples were grinded before the beginning of the testing phase. It was also observed that the values taken for un-grinded samples were higher than the grinded ones. This is due to the improper definition of the failure criteria to the machine as samples already starter having

surface cracks which reduced the sensitivity range of the machine. The tiny scratches lower the reaction force of the specimen making the detection of fracture harder for the machine; thus, the machine can continue working and counting number of cycles even the specimens were already broken.

The machine assembly shown in Figure 3.30 was used for the cantilever bending test. It consists of an electric motor attached to an eccentric crank in which the rocker arm is attached connecting the specimen stage (Figure 3.34) to the motor. The 0.5 HP motor can deliver up to 40 Ib of force (178 N) through its rocker arm to the specimens. The specimen stage consists of 4 specimen slots each has two adjustment screws above and below the load cell.
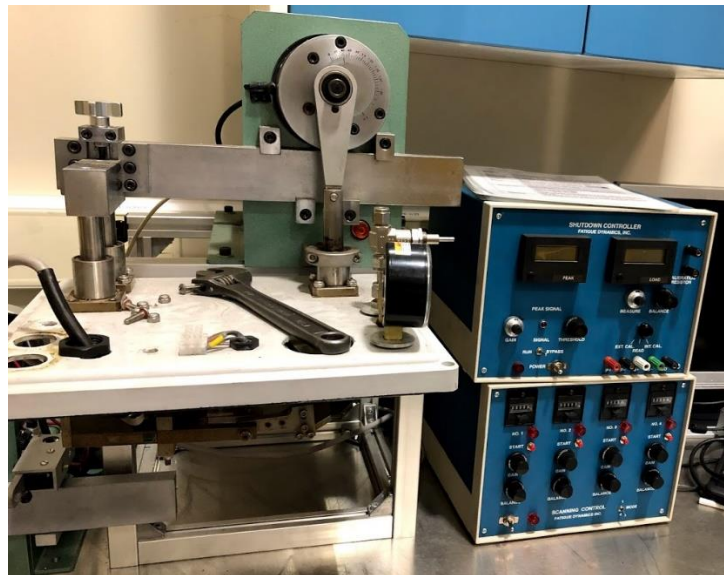
Figure 3.30:   Flexion fatigue machine.

The machine is controlled by means of a shutdown controller and a scanning controller. The shutdown controller shown in Figure 3.31 is responsible of sensing the failure and fracture of the specimen and transmitting the signal to the scanning controller (Figure 3.32) to stop counting for this specimen. It consists of four knobs (Gain, Threshold, Measure and

Balance), two selectors (Run-Bypass and Ext.Cal-Read-Int.Cal) and a power switch, it also contains some connectors for the external calibration of the machine. Two dials are which are the Peak and Load dials are presented at the top of the controller and a red indicator referring to reaching the desired peak is located between the Gain and Threshold knobs.

Figure 3.31:   Shutdown controller of bending fatigue machine.

The scanning controller on the other side is responsible of counting the number of cycles for each channel separately. It responds to the signal delivered from the shutdown controller to deactivate the counting of certain channel upon reaching the desired peak (failure of the specimen in this channel). It consists of four counters for the four channels, four reset and start buttons for each channel and four lamps indicating the deactivation of each channel. It also contains four balance knobs and four gain knobs for each channel, and a mode selector located at the bottom left of the controller beside the ON-OFF switch.

Figure 3.32:   Scanning controller of bending fatigue machine.

The setup and start-up of the machine is a little bit complicated and the instruction list should

be revised for each operation to ensure that there is no step has been forgotten. The setup

takes the following steps according to

Table 3.1:   Setup of cantilever bending fatigue machine.

Step	Description of task
1. Sample preparation	Samples should be prepared according to Figure 3.25.
2. Connection and verification of mounting.	All wires should be connected according to Figure 3.33.
3. Start-up of the device.	Open the 'ON-OFF' switches for both the scanning and shutdown controllers.
4. Shutdown controller adjustments.	Adjusting the 'Balance' knob at the center and setting the 'Measure' knob to 500. Selector to 'Bypass'.
5. Scanning controller adjustment	Make sure all counters are set to zero and all red indicators are turned off. 'Mode' selector should be on mode 4. (Mode 1 makes the machine stops after the first failed specimen while mode 4 only stops the machine if all the 4 specimens break).
6. Resetting first load cell.	Press the Channel selector button at the back of the scanning controller until the counter of channel 1 is incremented by ½ turn. Adjust the 'Balance' wheel at the center by turning clockwise or anticlockwise. Adjust the 'Gain' wheel to maximum gain (to the end turning anticlockwise).

		Make sure that the selector is on the 'Read' position and adjust the 'Balance' wheel till the value of the load dial reaches 0.
7.	Internal calibration of load cells.	Move the display selector to 'INT CAL' position and adjust the 'Measure' knob so that the value on the load dial is as follows [46]: Channel # 1 = 28.0 LB-IN Channel # 2 = 27.8 LB-IN Channel # 3 = 27.7 LB-IN Channel # 4 = 27.3 LB-IN Return the display mode selector back to 'Read' ensuring that the value of the load display dial is still 0. Lock the 'Balance' wheel with the locking mechanism.
8.	Installing of first specimen.	Install first specimen in channel #1 and tighten the fixation bolt as well as the roller guides (Figure 3.34).
9.	Adjustment of stroke of rocker arm.	Loosen up the four bolts and adjust the fifth to the desired value, then, re-tighten the four bolts to lock it in place.
10.	Adjustment of load cycle.	Because each specimen has a little tolerance in dimension than the other, it is important to adjust each channel so that the sinusoidal load cycle is the same for all samples. In the case of this project a complete reversible cycle is required so the maximum positive load should be equal to the minimum negative load. To do that, rotate the motor spindle by hand till the load dial reads the maximum value. Do the same for the minimum negative load adjusting the adjusting screws above and below the load cell till having the same load value for the positive and negative loads.
11.	Adding the other specimens	Repeating steps 6 through 10.
12.	Motor start-up	Press the 'Start' button on the electric motor and adjust the speed by turning the speed wheel from 4 to 40 Hz. (expressed in relative percentage).
13.	Adjustment of failure criteria of specimens.	While the motor is running, adjust the 'Gain' knob for specimen one at the center and adjust 'Gain' knob on the shutdown controller so that the peak dial represents 100. Adjust the Gain knob in the scanning controller for the others specimens so that the peak dial represents 100 too (waiting for the channel to be switched automatically). Adjust

	the failure criteria by lowering the peak by a fraction of the maximum peak e.g. 75% by decreasing the 'Gain' knob in the shutdown controller and rotating the 'Threshold' wheel so that the peak indicator is just on. Adjust the 'Gain' wheel back to 100%.
14. Running the test.	Set the selector on the shutdown controller to 'Run' otherwise the machine will run indefinitely.
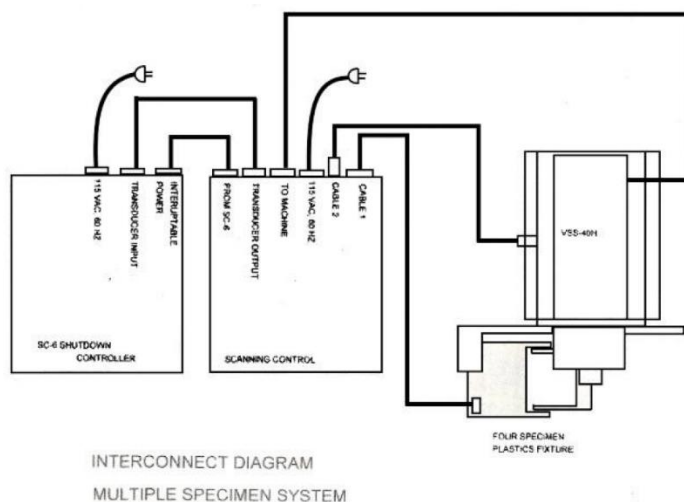
Figure 3.33:   Connections schematic diagram for bending fatigue testing machine.
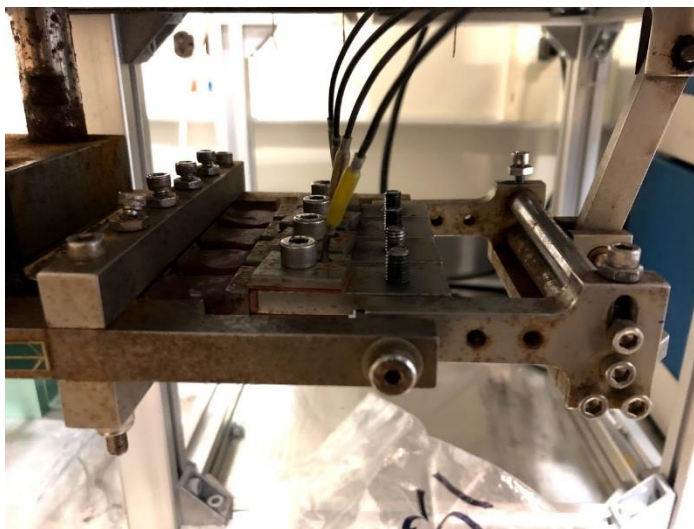
Figure 3.34:   Samples stage showing the place for four independent specimens.

The scanning controller counters have a sensitivity of 1000 cycles as the controller can only work on each sample separately. The controller works by checking the condition of the sample and if it is still above the failure criterion the controller counts 1 and moves to the next channel after an amount of time depending on the rotational speed of the motor. The motor can rotates with frequencies from 4 to 40 Hz by turning a knob marked from 0 to 100%. The conditions set for this particular test was 12 Hz as very high speeds can result in untighten bolts which result in the failure of the test. The deflection selected was 0.25 in. (6.35 mm) for all samples including dummy samples. Selection was based on trial of more than deflection value and comparing the corresponding fatigue life. The stress induced in the specimen was calculated using the Matlab code explained below:

1. First part is the inputs based on the material characteristics and specimen dimension. For aluminum, E = 70 GPa and υ (Poisson's ratio)=0.3, while the specimen dimensions were as described in Figure 3.25.

```matlab
%% Material definition
E=70000; %MPa
n=0.3; %poissions ratio
%% Specimen definition
L=63.5; %mm total length
W=19; %mm maximum width
w=4.57; %mm minimum width
t=3; %mm thickness
h=t/2;
```

2. Definition of vectors to store the outputs of each loop step. Step was selected to be 0.1 mm for high accuracy.

```
%% Calculations
d=6.35; %deflection in mm
i=0.1; %loop step in mm
stress=zeros(1,L/i);
bb=zeros(1,L/i);
ii=1;
```

3. Stress calculation inside for loops using solid mechanics formulas $I = \frac{bh^3}{12}$ and $\sigma = \frac{My}{I}$, where I is the 2nd moment of area, b is the specimen width, h is the specimen thickness, σ is the stress, M is the maximum moment and y is half the thickness. Specimen was divided into for parts each with a separate for loop, below is an example of two for loops.

```
for x=0:i:19.5
    b=W;
    I=(b*h^3)/12;
    F=0;
    M=F*(L-x);
    s=M*h/I;
    stress(ii)=s;
    bb(ii)=b/2;
    ii=ii+1;
end
for x=19.6:i:26.7
    z=26.7-x;
    a=tand(45)*z;
    b=2*a+w;
    I=(b*h^3)/12;
    F=(d*(L-x)^3)/(3*E*I);
    M=F*(L-x);
    s=M*h/I;
    stress(ii)=s;
    bb(ii)=b/2;
    ii=ii+1;
end
```

4. The final step is to plot the results and specimen profile in order to illustrate location of maximum stress visually.

```
%% Plotting
bb(ii-1)=0;
bb(1)=0;
x=[0:i:L];
subplot(2,1,1)
plot(x,stress,'k')
subplot(2,1,2)
plot (x,bb,'r')
hold on
plot (x,-bb,'r')
```

The result of this code is a plot showing the variation of stress throughout the specimen length and showing the specimen profile below the stress plot of better visualizing. Figure 3.35 shows the resulting plot of the code showing a maximum stress of 50 MPa at the center of the reduced width area, stress then decays reaching zero near both the restrained and the free ends.
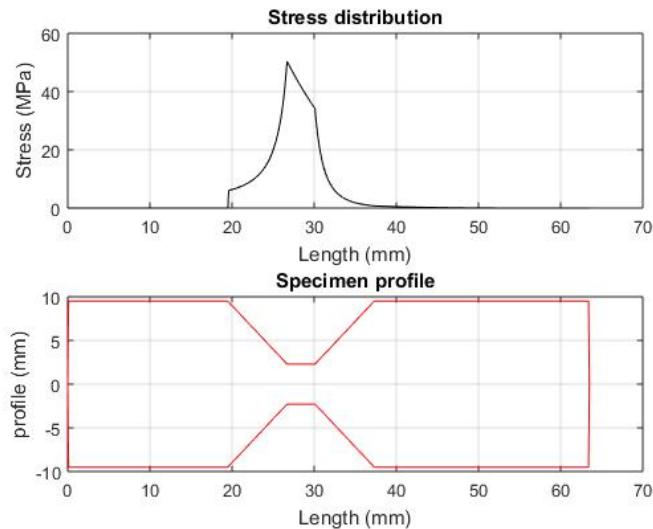
Figure 3.35:   Stress distribution plot of cantilever bending machine.

3.5   Finite elements verification of previous design modifications

The literature in previous section proposed different designs of the control arm that showed enhancement in terms of their castability. These designs were simulated to adapt semisolid

casting technique avoiding the formation of voids during casting. A finite elements simulation using Abaqus was performed on the previous proposed design in which the maximum Von-Mises stresses for all of them were found to be higher than the conventional design of the control arm. The masses of the proposed design were also higher than that of the conventional design which indicates a decrease in performance for the new designs. As this study aims in producing a superior control arm design in terms of the stress distribution as well as a remarkable decrease in its total mass; the proposed design from literature were used to observe their weaknesses and improve them. Therefore, it was important to simulate the previous recommended designs in order to unify the comparison criteria between the designs proposed in this study and those of literature. There are many forms of dissimilarities that can be found in finite elements simulation. These dissimilarities can take the form of different boundary conditions, different load application, different elements size, different elements type, and many other factors. As a result, a difference between the simulations is expected and is important to find in order to be able to compare these designs to the new developed designs. This subsection will cover the discussion of each proposed design by the literature, as well as, the validation of the finite elements simulation for each and calculation of the error between values.

3.5.1 Conventional design

Finite elements analysis (FEA) of literature was done using Abaqus 6.13 with an element size of 4 mm which corresponded to total number of elements from 74,000 to 102,400 elements (for all designs) and a total number of nodes ranging between 16,200 to 22,679 nodes [40]. A force of 5.5 kN was applied at the end of the control arm by means of adding

additional shoulders in the ball joint location in which the load was applied on. The method of force application may not be completely matching real loading conditions due to the addition of an excess material to the control arm.
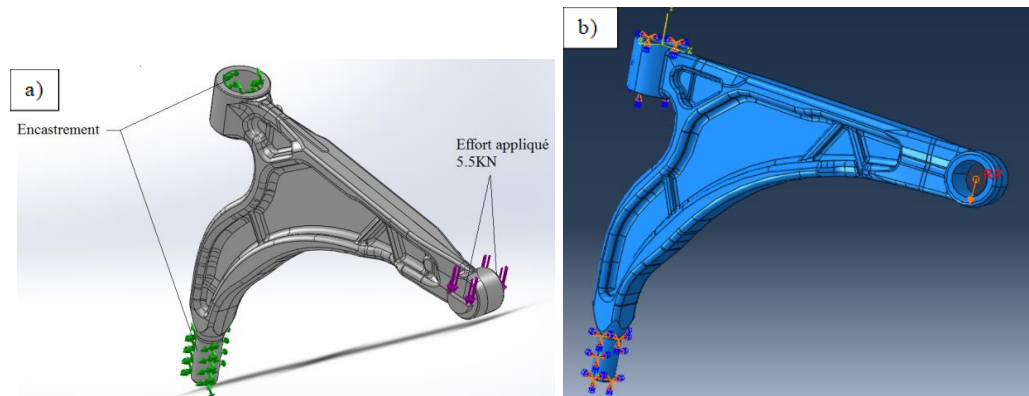
Figure 3.36:   Method of force application by the FEA. a) Method of literature [40], b) method in this study.

The part takes the form of a middle web attaching the upper and lower flanges to make the form of an I-section throughout the cross-section of the part as shown in Figure 3.37. The simulation of the conventional design of literature shown in Figure 3.38a revealed a maximum Von-Mises stress of 193 MPa near the upper and lower bushing areas (Figure 3.36).
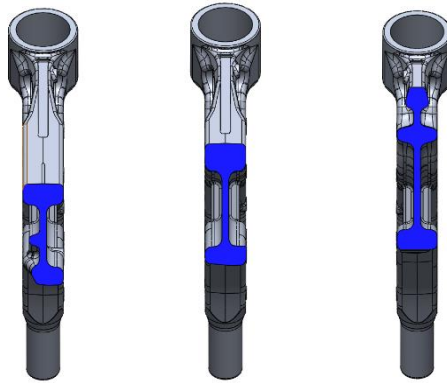
Figure 3.37:   Cross-section of conventional design.

The validation of the FEA of literature was done using Abaqus finite elements package with an element size of 3.5 mm which corresponded to a total number of 109,561elements. A Force of 5.5 kN was applied on the reference point 'RP', which is attached to the inner surface of the ball joint location by means of a multiple point constraint (MPC). The MPC is a beam attaching the inner surface of ball joint to the reference point. It is used to better simulate real loading conditions and minimize the error percentage. The results revealed a maximum Von-Mises stress of 232 MPa near the same locations of proposed by the literature as shown in Figure 3.38b. The total displacement was found to be around 1.4 mm at the end of the control arm. The error value was calculated to be 20.2% between literature and the FEA in this study. The large error is due to different element size as well as the difference of force application between literature and this study as illustrated in Figure 3.36.
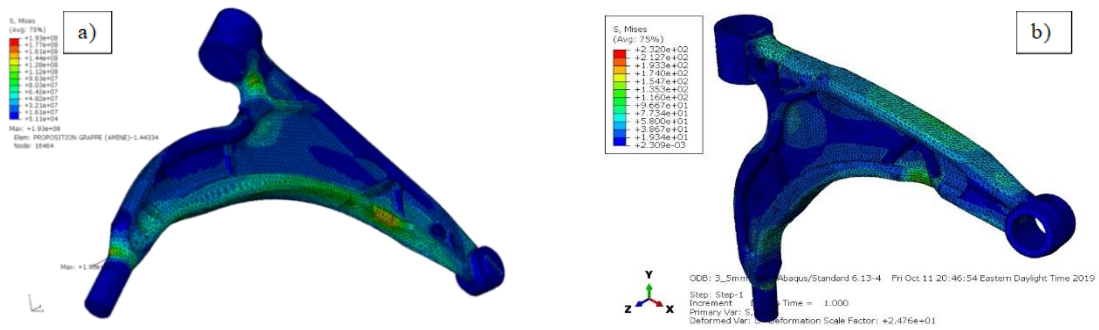
Figure 3.38:   Finite elements analysis of conventional design. a) result from literature [40], b) validation of literature.

3.5.2   Z-Shaped design

The FEA of literature was done as described above with same element size and total number of elements using Abaqus 6.13. The design consists of an inclined mid-web taking the form of a Z-shape throughout the cross-section of the part as shown in Figure 3.39. The total mass of this design is 1227 g calculated using the SolidWorks mass evaluation tool.
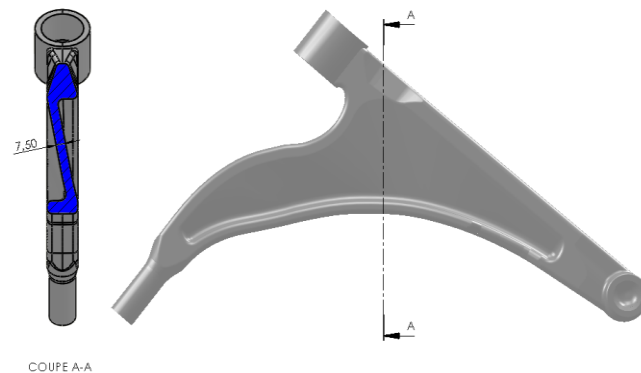
Figure 3.39:   Cross-section of Z-shaped design [40].

The results of the literature FEA is shown in Figure 3.40a, showing a maximum Von-Mises stress of 199 MPa near the location of the upper bushing. The validation of this design was done using Ansys 19.1 with an element size of 2 mm, and a maximum Von-Mises stress of

234 MPa was observed near the upper bushing location. The error value between the two simulations is found to be 17.6% which is considered very large.
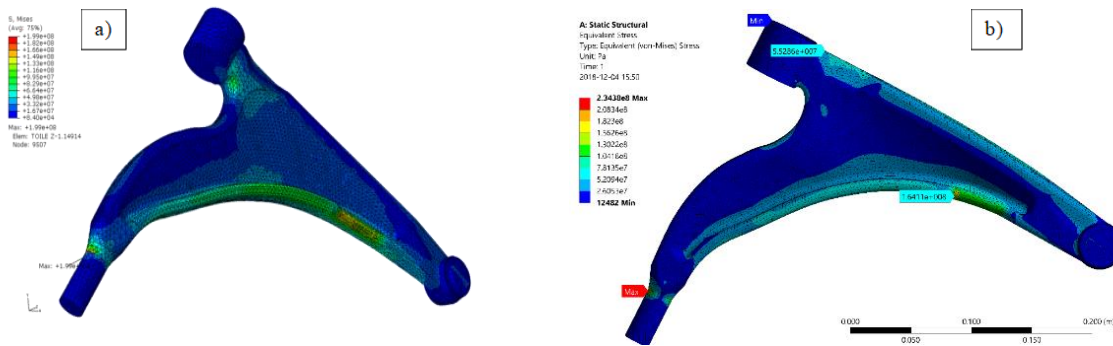
Figure 3.40:   Finite elements analysis of Z-shaped design. a) result from literature[40], b) validation of literature.

3.5.3   Mid-Reinforced design

The finite elements simulation was performed using the same conditions described above. The design focuses on reinforcing the mid-section of the control arm to become more rigid in this region as shown in Figure 3.41. The total part's mass was calculated to be 1222 g using SolidWorks mass evaluation tool given the density of aluminum A357 as input.
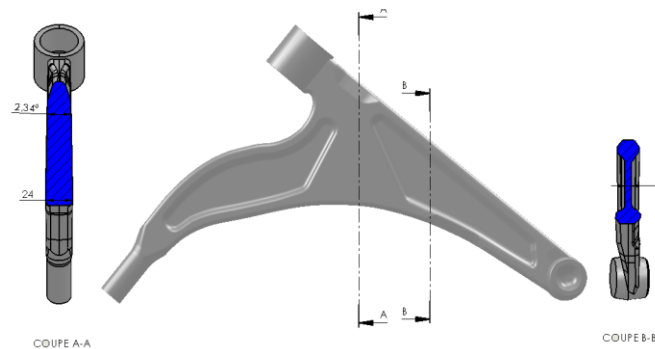
Figure 3.41:   Cross-section of Mid-Reinforced design [40].

The FEA of literature (Figure 3.42a) revealed a maximum Von-Mises stress of 209 MPa located near the same location as previous designs. The validation of this simulation was performed using the same conditions mentioned above using Ansys 19.1. The results, shown in Figure 3.42b, show a maximum Von-Mises stress of 204 MPa near the same location as that found by literature. The values of this simulation match that of literature with an error percentage of only 2.4%.
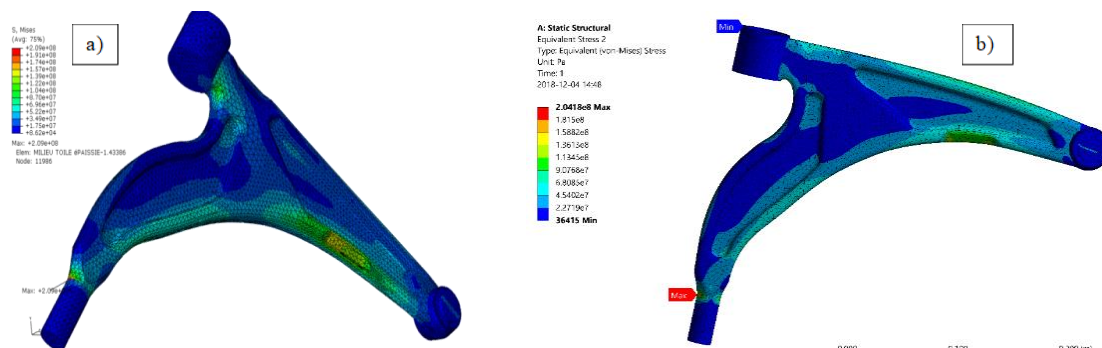
Figure 3.42:   Finite elements analysis of Mid-Reinforced design. a) result from literature [40], b) validation of literature.

The final recommendation was the Z-shaped according to its better castability than the conventional design that was observed to have points of flow turbulence during casting.

3.6   Design modifications and finite elements

The design of the control arm has an important role in transferring the force to the ball joints. A good design of the control arm will not only increase the life of the part itself, but also the life of the ball joints which usually wear faster. The current design of the control arm shows high stress regions in which fracture is predicted to happen. To figure out a better design 16 designs were proposed following the recommendations of the literature while decreasing the

weight of the part as much as possible. The simulations of these parts were done to best match the real operation and loading conditions by selecting the proper finite elements setup.

3.6.1 Setup of finite elements and idealization of problem

Finite elements analysis (FEA) was performed using Abaqus CAE 2018 finite elements package. Aluminum material was defined manually using a Young's modulus (E) of 70 GPa and a poission's ratio (υ) of 0.3 for an isotropic material. Other properties like density, thermal conductivity, etc., are not important in this problem; as a static simulation is done where E and υ are the only unknowns in the stiffness matrix. A solid-homogenous section was created and assigned to the imported body of each control arm design. A reference point (RP) was created at the center of the ball joint location at the tip of the control arm. This reference point (RP) as used in the multiple point constraint (MPC) beam interaction to connect the inner surface of the ball joint to RP (Figure 3.43c). A load of 5500 N was then applied to RP with a magnitude of -5500 in the y-direction (F2) as shown in Figure 3.43a. Elements type was selected to be 3D tetrahedral elements with size from 2 – 3mm which corresponded to elements ranging from 350,927 to 121,081 elements. Meshing was verified by the element verification tool and the major aspect ratio was set to be 0.85 as shown in Figure 3.43b.
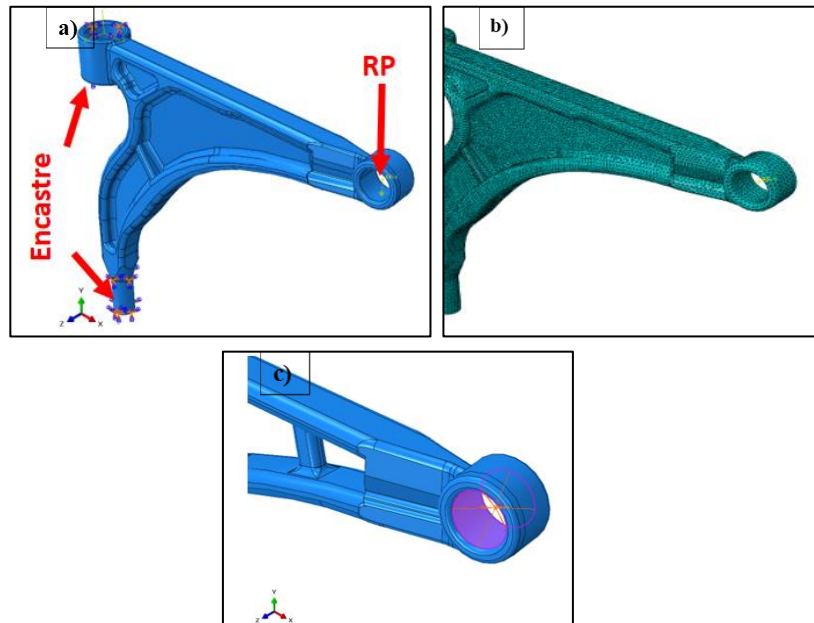
Figure 3.43:   Finite elements configuration. a) boundary conditions, b) meshing of the control arm part, and c) the multiple point constraint (MPC) interaction.

The MPC beam represents the most appropriate loading condition to be most similar to real loading conditions. Among the 16 designs, four designs were selected that possesses good performance and shows the effect of change of design which are described below.

3.6.2   Design 1: Inclined web with reinforcement ribs

The design of the control arm obliges the ball socket to be inclined to the body of the control arm. This inclination causes inhomogeneity in the lower flange of the control arm; raising the stress at the outer regions and causing stress concentration regions. An inclination of the web is believed to cancel the effect of ball socket inclination and decreasing the maximum stress in this region. On the other side, inclination of middle rib may weaken the structure of the control arm requiring the presence of reinforcements in some particular regions.

This design followed the recommendation of the literature as it proposed using an inclined Z-shaped web instead of the conventional straight design. Web inclination was set to be 7° relative to the normal of the plane parallel to the upper flange as shown in Figure 3.44 to compensate the 5° inclination of ball socket. The angle of inclination was selected after multiple trial and errors using different angle each time and carrying out FEA simulation.
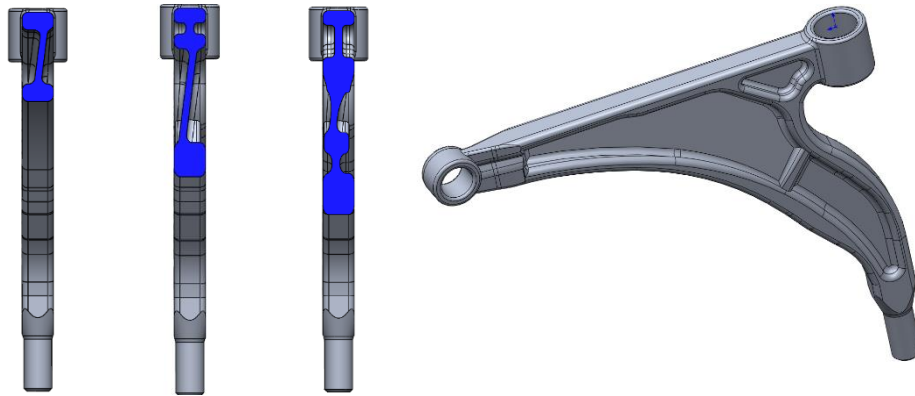
Figure 3.44:   Design 1: Inclined web with reinforcement ribs design.

The structure was reinforced by means of a small rib at the lower part of the control arm to limit excess deformation under load. The total mass of the part was found to be 1198 g, which is nearly similar to that of the conventional design (1200 g).

3.6.3   Design 2: Planar thin web

The thin web design is the most basic design in the critical thinking of manufacturing of the part; due to is simple design. The design eliminates the use of any reinforcement ribs and increases thickness of the upper and lower flanges in critical stress regions[5]. The middle web

---

[5] Regions where fracture was observed in the conventional design hydraulic testing and that was predicted by the finite elements simulation.

has a thickness of 4 mm as shown in Figure 3.45 which decreases the total mass of the control arm to 1141 g (less by 59 g than the conventional design. The decrease of weight is not considered enough for performance improvement; thus, elimination of more material is required.
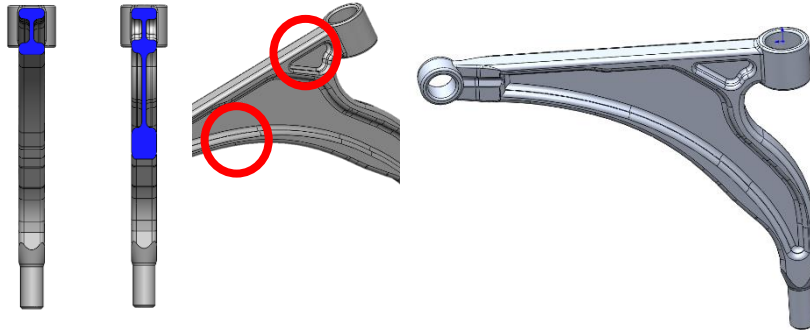
Figure 3.45:   Design 2: Planar thin web.

3.6.4   Design 3: Hollow design

The hollow design is the evolution of the previous design with the removal of materials where zero or little stress was observed as shown in Figure 3.46. One rib was added to the lower part of the control arm to increase the rigidity of the control arm in this critical region.
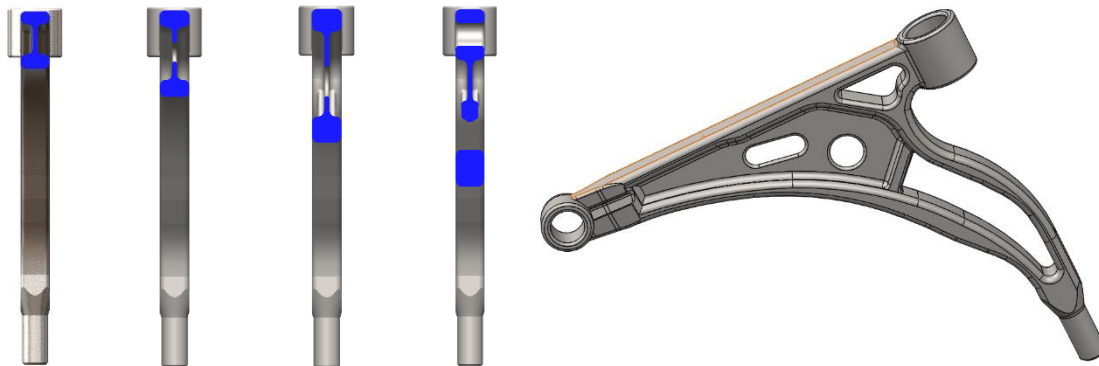
Figure 3.46:   Design 3: Hollow design.

The total mass of the structure was decreased to 1082 g; however, stress concentration regions are expected to occur near the hollowed regions which may cause easier fracture.

The formation of these stress concentration regions is due to the presence of holes in the web of the control arm. Therefore, a renovation of this design was needed that has the advantage of weight reduction without the use of pierced web. The solution of this problem was found by the developed of the succeeding design.

3.6.5   Design 4: Trussed design

The trussed design was developed to solve the issue of stress concentration due to web piercing; thus, this design replaced the middle web with a number of ribs as shown in Figure 3.47. 5 ribs were developed to withstand the loading conditions and to connect the upper and lower flanges of the control arm. The idea of the design is to increase the flexibility of the control arm structure thus ensuring that the stress is distributed evenly throughout the whole part. The shape, number, dimensions and locations of the ribs were selected after multiple trial and errors to compromise the weight and performance of the part. The trussed design is the lightest design weighting only 1040 gm making it the most efficient design in terms of weight.
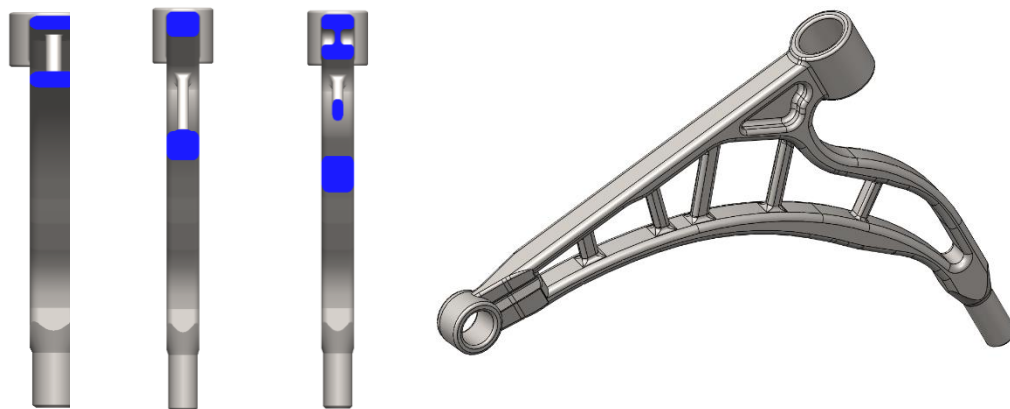
Figure 3.47:   Trussed design.

The design resembles the shape of trusses found in many structures as bridges and steel buildings; hence, its name comes from. The idea of the design is based on removing excess material and distributing loads on the whole structure of the control arm rather than the concentration of stress in particular regions and zero stress in others.

The results of the FEA simulations are included in the results and discussions section in which a comparison between the four proposed design as well as the conventional design will be found at the end of this section.

Chapter IV

Results and discussions

4. Results and discussions

This chapter presents and discusses the results of the experimental work explained in the previous chapter. The data presented in this chapter represents the real order of experimentation, which was applied in the decision making of the following experiments. The first approach in the experimental work was the tensile testing, as it is considered one of the most reliable and important testing methods in which its results can be easily compared to literature. The evaluated data of tensile were used in the planning of the fatigue experiments which are applied on the applicable control arm parts and standard fatigue specimens using servo-hydraulic machine and the cantilever bending fatigue, respectively. In parallel, design modifications and finite elements analysis (FEA) were in progress which aimed in developing a qualified automotive parts of lower suspension arm in terms of weight and stress distribution. The experimental and analytical works were combined to arrive at the best design and thermal treatment, as well as, the expectation of total fatigue life by applying the best thermal treatment to the most significant design.

4.1   Tensile properties

The results of the tensile data are shown in Figure 4.1 representing the average value of each property (either elongation, UTS or YS). Elongation percentage (%E) is represented as bar chart with values presented at the left y-axis of the figure in percentage values. Yield strength (YS) and ultimate tensile strength (UTS) are represented by means of scatter lines having blue and red colors of YS and UTS respectively. The values of both YS and UTS are presented at the right y-axis of the plot in Mega-Pascals (MPa).

It can be observed that solution heat treated (SHT) specimens show significantly higher ductility (23%) than all other aging cycles, however, the yield strength is observed to have the lowest value of 136.6 MPa.

The under-aging cycle WA0 shows the best elongation compared to other aging cycles (17.3%) with an improvement in the value of the yield strength of 201 MPa. The YS and UTS reach maximum values for the A-aging cycles, namely, WA1 aging cycle (YS = 201.5 MPa, UTS = 270 MPa) with the lowest %E among the A-aging cycles (7.6%). The YS and UTS decay continuously to minimum values of 191 MPa and 238 MPa, respectively, for WA8; while the values of %E rises to reach 9.3%.

Regarding B-aging cycles, a slight enhancement of strength values moving from WB0 to WB5 can be observed reaching a maximum YS value of 243.5 MPa at WB5 aging cycle. The maximum %E value is observed to be 10% for WB0 aging cycle, which also possessed the lowest strength values. A slight increase in strength values throughout B-aging cycles are noted, however, a significant change of ductility can be observed.

An increase in the strength values is observed for C-aging cycles from 272 MPa YS for WC1 reaching 288 MPa YS for WC3. On the other hand, the %E values decrease from 12% for WC1 to 9.4% for WC3. Aging cycle WC2 has moderate properties regarding strength and %E in between WC1 and WC3. A remarkable high strength can be observed for WC3 aging cycle having highest strength of all other aging cycles of 288 MPa and 302.8 MPa for YS and UTS, respectively.
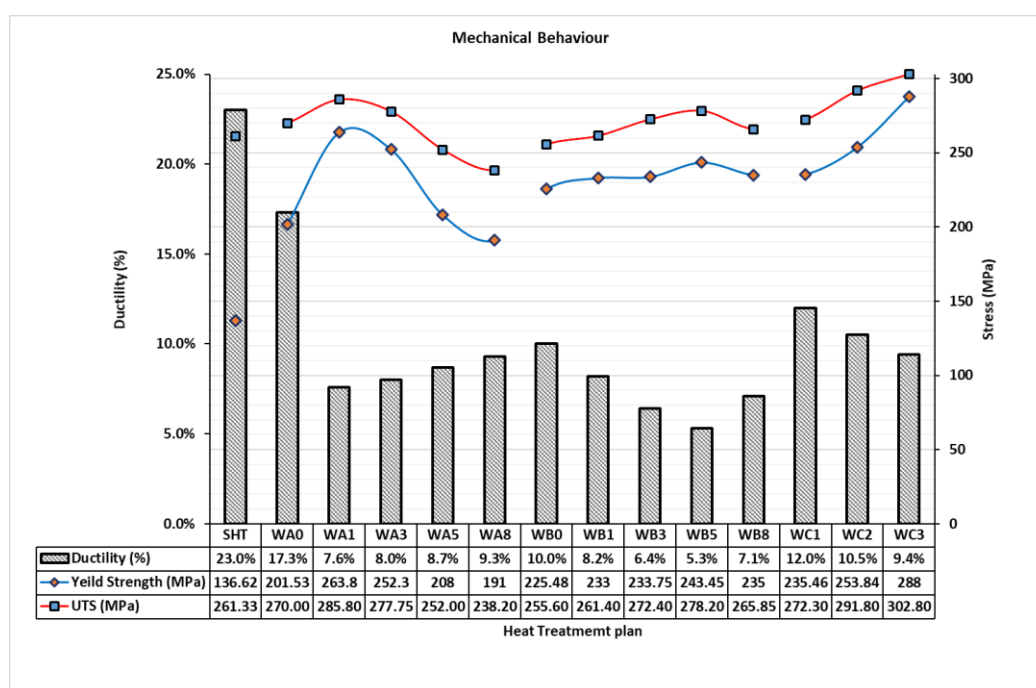
Figure 4.1:   Tensile properties chart.

The data shown in Figure 4.1 was evaluated and the best aging cycles in terms of strength and ductility were selected to proceed for studying its effect on the fatigue performance. The effect of the multi-step thermal aging is shown from the results of YS, UTS and ductility verifying the conclusions of previous studies on similar multi-step aging cycles [31,32,47].

4.2 Fatigue performance of lower control arm

The results of fatigue are shown in Figure 4.2 indicating the number of cycles till failure for specific aging cycles investigated. As mentioned previously, samples are considered as defected and rejected if the fracture was observed outside the expected zones. Red marked bars (WA1, WB5) represent the defected samples that were rejected, and its results cannot be used in comparison with others. The standard T6 aging condition is represented by the green bar and is used to be compare with the other aging cycles.

A slight enhancement in the total fatigue life can be observed for the aging cycle WA0 showing an increase of 4,000 cycles over the standard T6 thermal treatment. The improvement is not very remarkable for this aging cycle, however, WA0 is considered to be more economical than T6 with only 2 hours of aging compared to 6 hours for T6. WC3 shows significantly the highest number of cycles compared to other aging cycles by having a double fatigue life of T6 condition (72,000 for WC3 versus 36,000 cycles for T6 conditions). The results reveal a good trend matching the results of the tensile testing, as well as, those mentioned by previous studies done concerning fatigue of A357 alloy [48–50].
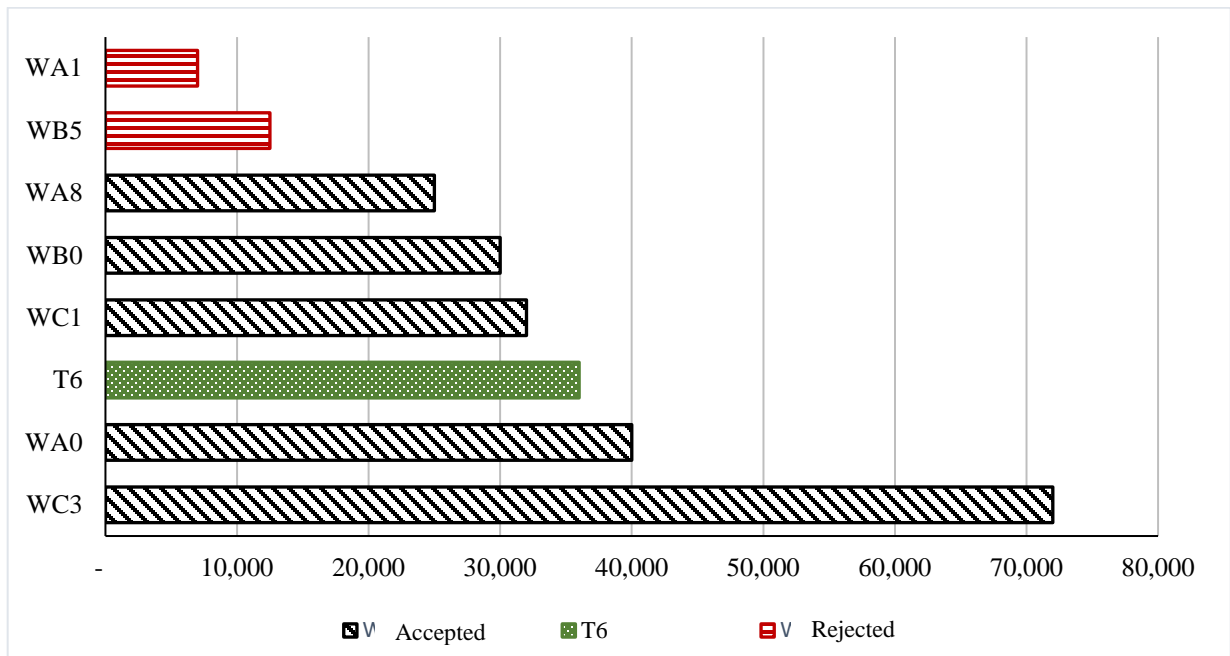
Figure 4.2:   Real part low cyclic fatigue bar chart.

No other improvement can be observed for other aging cycles, however, WA1 which showed very good tensile properties; its sample was detected to be defective. Due to the limited number of semi-solid casted applicable control arms; the repetition of the experiment was not possible. As a result, the cantilever bending fatigue specimens were used in this study.

4.2.1   Fractured surface analysis using scanning electron microscopy (SEM)

The SEM micrographs of the fracture surface of investigated samples of control arm are shown in Figure 4.3. The figure indicates the type of fracture either ductile or brittle for various thermal aging cycles investigated.

For samples of WA0 and WC3 slip bands and beach marks were observed indicating a complete fatigue failure and the absence of defects. In addition, the presence of dimpled structure for both WA0 and WC3 samples indicates a ductile failure due to fatigue. A nearly defects-free

microstructure for WC3 with the presence of slip bands and dimpled structure causing a ductile fatigue failure can explain the high number of fatigue cycles for this sample[51].

Porosities were observed for the WA1 and WB5 samples hence it was rejected due to its very low fatigue life cycles. In addition, the WB5 showed the presence of oxides in aluminum matrix which has negative effects on the microstructure characteristics and fatigue performance of alloys investigated. These defects may highlight the problems and difficulties related to the semi-solid casting technique, that requires high precision and sophisticated equipment.

For the control arm sample of WB0, the microstructure observed indicates a fatigue failure that with a brittle structure. This brittle microstructure indicates an inductile material; hence, the crack propagation was very fast that slip bands could not be clearly observed as those in WA0 and WC3 samples.

The results revealed by the SEM of the fracture surface of semi-solid casted control arm marks the importance of the absence of major casting defects that have a direct effect on the fatigue life. The SEM imaging confirms the study done by Nadot et al [42] for the reason of failure due to different casting defects. The results also marks one of the disadvantages of semi-solid casting, which is the requirement of sophisticated machinery to regulate the temperature of the metal paste to limit the presence of macro-porosity in casting.
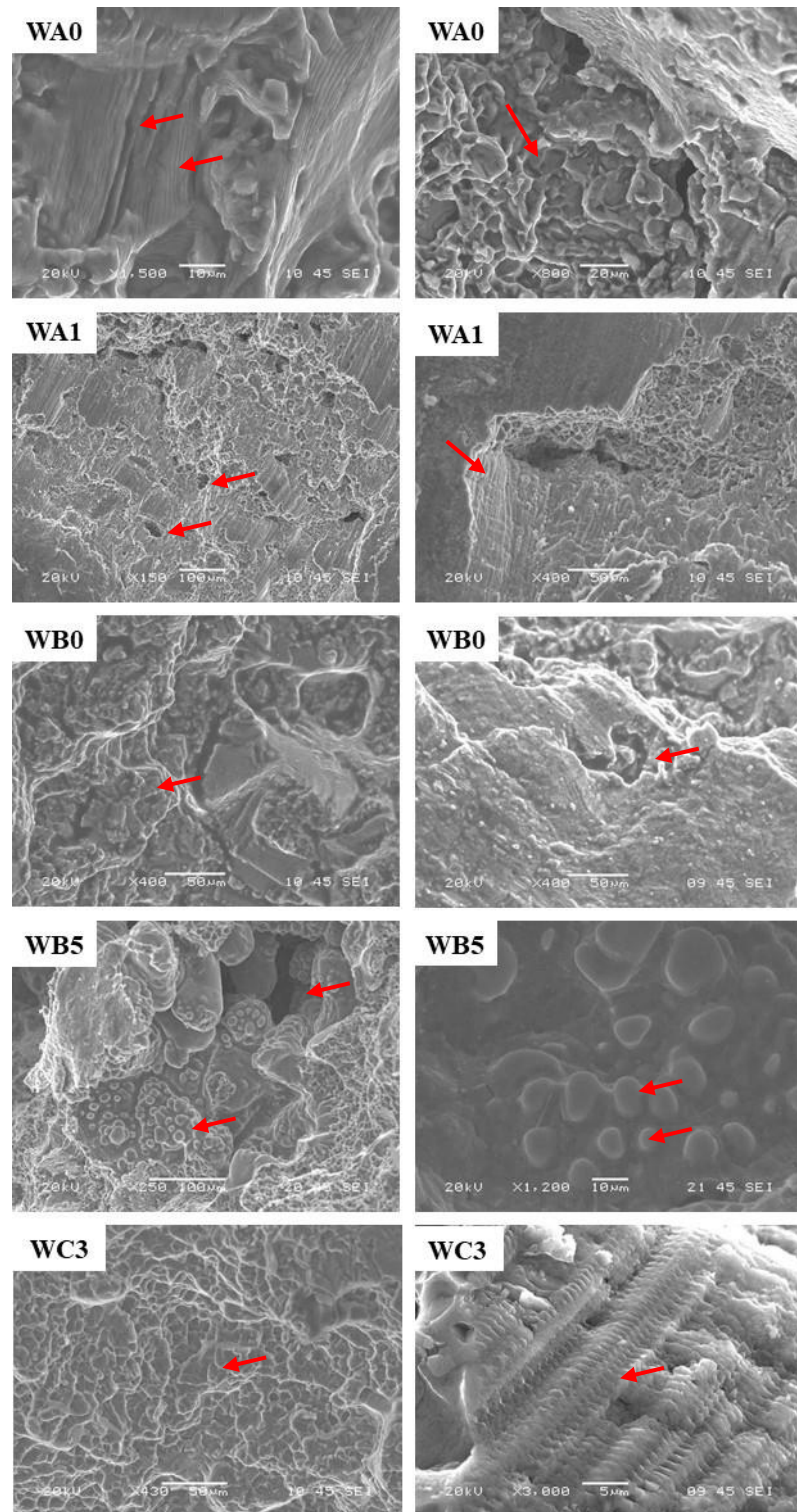
Figure 4.3:   SEM imaging of the fracture surface of some control arm samples.

4.3   Constant deflection cantilever bending fatigue results

The cantilever bending fatigue test was setup as explained in the previous chapter; the results of all test specimens were recorded. A visual inspection was applied for each fractured specimen to detect whether defects can be observed in the fractured surface. Figure 4.4 shows two fractured test specimens where defects can be clearly observed in Figure 4.4a. Black spots indicating the presence of porosities or oxides can be observed in Figure 4.4a, in contrast to the defects-free specimen shown in Figure 4.4b. These defects affect the fatigue life of the specimen and can be clearly noted by the value of the total fatigue life of this specimen. Defected specimen values were eliminated from the beginning and were not plotted nor used as a valid data point.

Figure 4.4:   Fractured fatigue specimens after testing. a) Defected specimen and b) defects-free specimen.

Accepted fatigue specimen values were plotted in the chart shown in Figure 4.5 and a moving average spline was fitted between the original test values. As observed, each aging condition was implied 3 to 4 valid points as other test values where discarded as they were detected as defective.

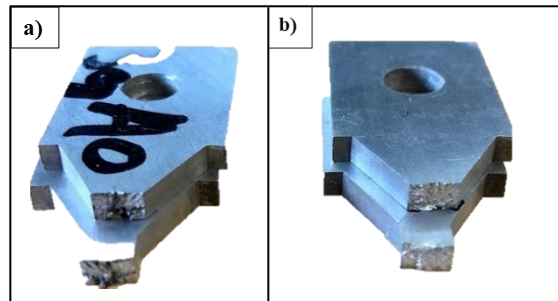The results reveal a remarkable increase in the fatigue life of WC3 aging cycle compared to the standard T6. The bending fatigue data validate the results of the real part fatigue testing explained previously (Figure 4.2) and the results of the tensile testing (Figure 4.1).
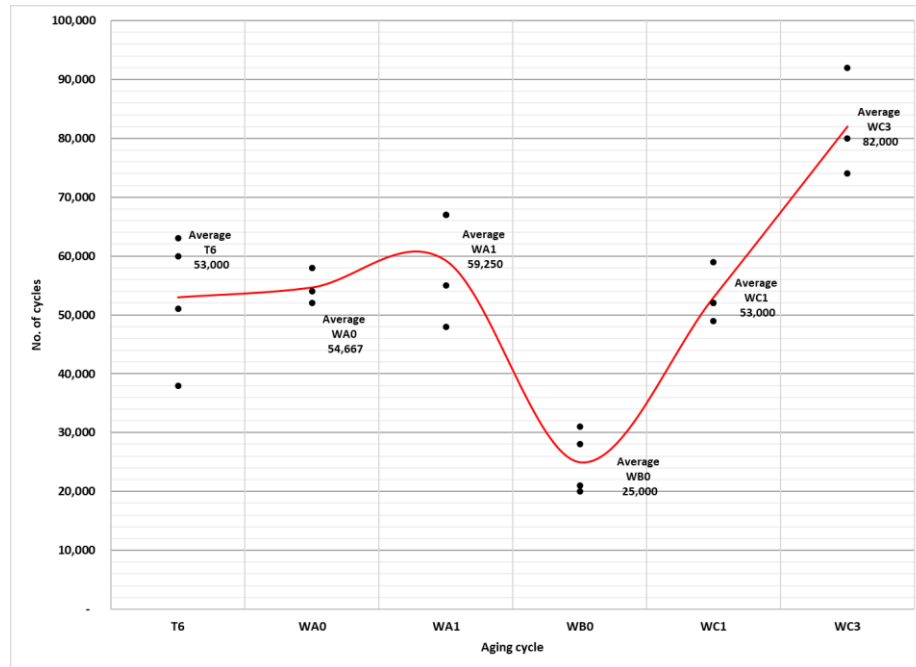
Figure 4.5:   Results of cantilever bending fatigue test.

Aging cycles WA0 and WC1 show nearly similar average fatigue values of 54,667 and 53,000 cycles, respectively, compared to the standard T6 with 53,000 cycles. On the other hand, aging cycle WA1 (59,250 cycles) shows an enhancement of fatigue life compared to T6 which could not be confirmed by the real part fatigue as the part was defected. WB0 aging cycle induced lower tensile and fatigue properties than T6 with only 25,000 cycles which indicates low mechanical properties for all B-aging cycles. A remarkable 155% enhancement of fatigue life for WC3 with an average of 82,000 cycles which continues to prove the superior properties of WC3 compared to T6. WC3 is also considered to be more economical

than T6 with only 5 h of total artificial aging time compared to 6 h of artificial aging plus 8 h of solution heat treatment for the standard T6.

4.4 Finite elements analysis of design modifications

In this sub-section, the results of the finite elements analysis (FEA) will be discussed in detail. A table is found at the end of this sub-section comparing the results of the modified designs with that of the conventional design.

4.4.1 Design 1: Inclined web with reinforcement ribs

The results of the finite elements analysis of the inclined web design are shown in Figure 4.6. The maximum Von-Mises stress is found to be 213 MPa observed near the lower bushing of the control arm. A maximum stress concentration factor (SCF) of 8.0 is observed near the lower bushing region. The maximum deformation at the location of the ball joint is 1.45 mm under the 5500 N force. A homogenous stress distribution in the lower flange is observed as shown in Figure 4.6b as a result of the inclined web that compensated the inclination of the ball joint socket. The inclination of the web has proven to compensate that of the ball socket causing that homogenous stress in the lower flange and the absence of any stress raiser regions.

Figure 4.6:   FEA of inclined web design. a) Von-Mises stress plot, b) total displacement plot, c) cross-sectional stress distribution.

The whole design can be classified to be rigid with a moderate stress distribution behavior and moderate deformation under the applied load. The web inclination has influenced the stress distribution in the lower flange as predicted, which match the recommendation of literature.

4.4.2   Design 2: Planar thin web

The results of the planar thin web design shown in Figure 4.7 show a maximum Von-Mises stress of 199 MPa. A maximum SCF of 9.95 is also observed near the lower bushing of the control arm in the location of maximum stress. The planar thin web design has nearly similar maximum deformation to the first design of 1.46 mm. The stress distribution in the lower flange is not homogeneous as the previous design due to the straight middle web. A SCF of 3.725 is also observed at the location of the arrow shown in Figure 4.7c. The design is observed to have high SCF values despite of the lower maximum Von-Mises stress.
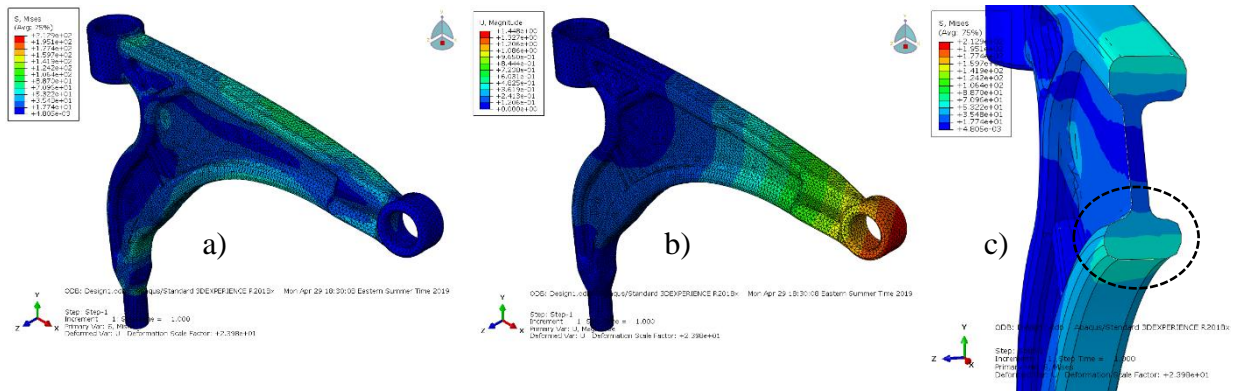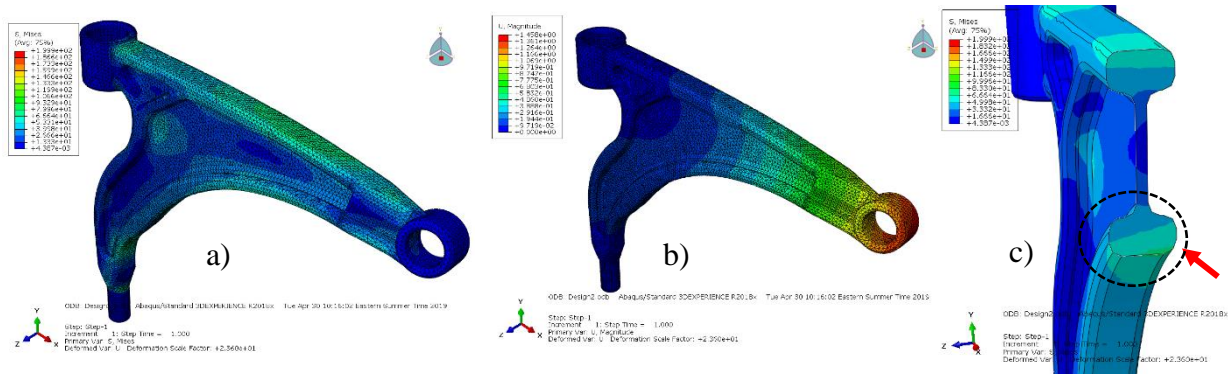
Figure 4.7:   FEA of planar thin web design. a) Von-Mises stress plot, b) total displacement plot, c) cross-sectional stress distribution.

4.4.3 Design 3: Hollow design

The FEA of the hollow design results are found in Figure 4.8. A maximum Von-Mises stress of 287 MPa is observed above the location of the lower bushing higher than the two previous designs. The maximum SCF decreased significantly to 5.2 despite the very high stress. The maximum deformation is observed to be 1.69 mm which is higher than all other previous designs. The high deformation and low SCF signifies that the stress is more homogenously distributed on the whole part. High stresses are observed near the locations of the holes marked with red arrows.
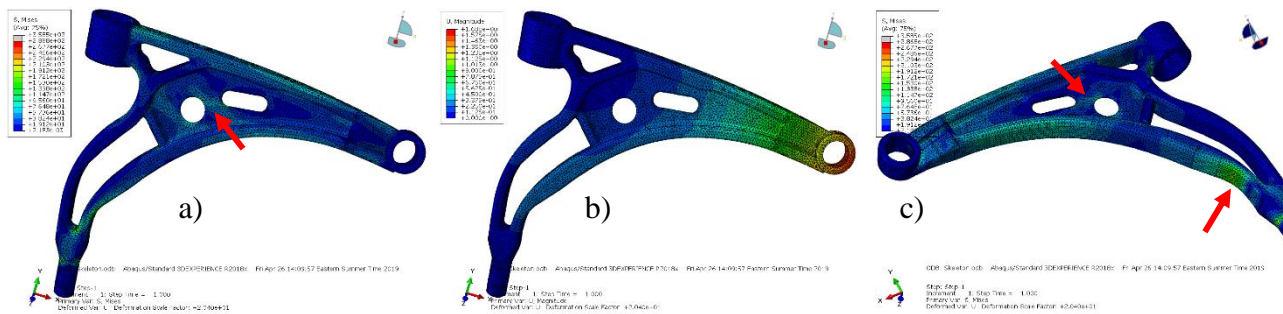

Figure 4.8:   FEA of hollow design. a) Von-Mises stress plot, b) total displacement plot, c) other view of VM stress plot.

4.4.4 Design 4: Trussed design

The maximum Von-Mises stress of the trussed design, shown in Figure 4.9a, is 198 MPa. A remarkable maximum SCF of 2.475 is observed indicating a complete homogenous distribution of stress over the whole body of the control arm. A maximum displacement of 1.78 mm is found at the location of the ball joint.
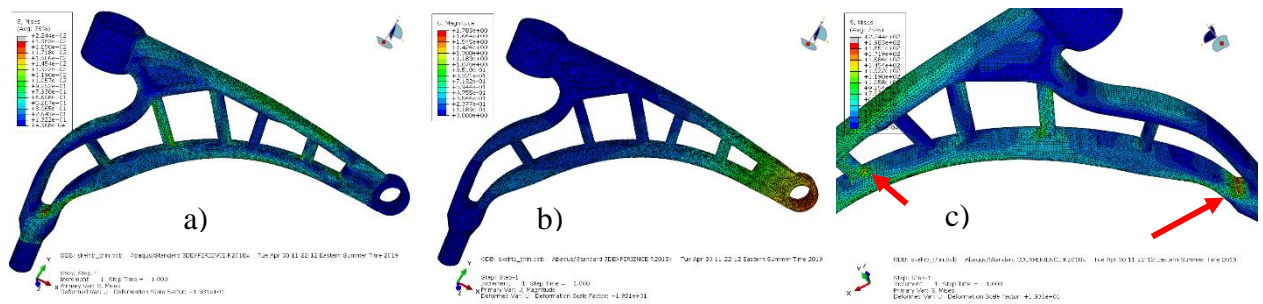
Figure 4.9: FEA of trussed design. a) Von-Mises stress plot, b) total displacement plot, c) other view of VM stress plot.

The maximum stress location is shifted from the previous designs and located near the location of the arrows. The design is less rigid than other designs and transfers the force evenly throughout the whole part.

4.4.5 Summary of FEA results

Table 4.1 shows a summary of the results of the four designs compared to the original design. The table represents the weight of each design, its maximum Von-Mises stress and its maximum deformation. An illustration of the percentage of improvement or deterioration of each value is presented under the values of both stress and deformation. The trussed design is observed to have the lowest maximum VM stress and the lightest weight. Percentages of enhancement is calculated and colored for the ease of comparison between different designs. Percentages were calculated by using the relation as follows:

$$Percentage\ of\ enhancement = \frac{Original\ value - New\ value}{Original\ value} \times 100$$

Table 4.1:   Summary of FEA results.

Part Name	Conventional design	Inclined web w/ribs	Planar thin web	Hollow	Trussed
Mass (g)	1200 O.D.M	1198 99% of O.D.M*	1141 95% of O.D.M	1082 90% of O.D.M	1040 86% of O.D.M
Max. Von-Mises stress (MPa)*	232	213 8.2% ↑	199 14.2% ↑	287 -23.7% ↓	198 14.65% ↑
Max. displ. (mm)**	1.4	1.45	1.46	1.69	1.78

* O.D.M = Original design mass.

** Stresses and displacement were calculated at 5500 N of force applied on the center of ball joint hole.

Chapter V

Conclusions and Recommendations

5. Conclusions and Recommendations

The results of tensile testing, control arm fatigue and cantilever bending fatigue emphasis the outstanding performance of the aging cycle WC3 than all other aging cycles. The WC3 aging cycle managed to outperform the T6 condition regarding strength and fatigue life. The WC3 aging cycle also has proven to withstand double the fatigue life compared to T6 condition which is a huge development in the industry of automotive components as suspension arms.

The results of tensile properties show that multiple interrupted aging cycle WC3 shows superior strength (YS=288 MPa) compared to other cycles. WC3 also shows a good ductility value of 9.4% compromising both strength and ductility in an economical aging cycle. WA0 also shows a remarkable compromise between strength and ductility and is more economical than the standard T6 heat treatment.

Aging cycle WC3 shows 100% enhanced of real part fatigue life than the standard T6 with 72,000 cycles for C3 compared to 36,000 cycles for T6. WA0 also shows enhanced low cyclic fatigue life of 40,000 cycles and as mentioned earlier is more economical than T6.

The results of cantilever bending test reveals superior fatigue life for aging cycle WC3 with an average of 82,000 cycles compared to an average of 53,000 for T6. These results confirm the results of the real part fatigue and prove the positive effect of WC3 on fatigue life. The aging cycle WA1 also shows enhancement over T6 with an average of 59,250 cycles, it is also considered to be more economical than T6.

Design 4 (Trussed design) shows superior properties than the original design. With a 160 gm lighter than the original design and a maximum VM stress of 198 MPa compared to 232 MPa

for the original design. Design 4 is also more flexible than the original design which can improve damping and increase the life of the ball joint connected to the control arm significantly. This flexibility is believed to better cushion road impacts resulting in better suspension behavior and comfort.

Applying the selected WC3 heat treatment to design 4 is expected to withstand more than 84,300 cycles[6] which is 134% enhancement of the part's life.

Recommendations for future work

The results and conclusions revealed in this study still needs more research to reach optimum design parameters, as well as, the application of the WC3 aging cycle in real road testing. In order to reach the best results regarding this topic a number of studies should be carried on:

- Run an optimization analysis using computer aided engineering (CAE) software to reach the optimum design. The modified trussed design can be used as a base for the optimized control arm with an objective function to minimize the total weight of the part.

- A computational fluid dynamics (CFD) analysis using software like ProCAST is needed to figure out the mold filling of the modified design using semi-solid casting parameters. This well help in proving whether the design is suitable for manufacturing or some modifications is required before manufacturing this part.

---

[6] Calculated by extrapolating the values of stresses of the original and new design with the values of T6 compared to WC3.

- Manufacturing of the optimized design and testing in real testing road conditions and the comparison with the conventional designs available in market.

References

[1]   D. S. Mackenzie, *Handbook of Aluminum*. 2003.

[2]   A. Tohru, G. Baker, C. Bates, T. Bell, and E. Bird, *ASM- Metals Handbook- Heat Treating*, vol. 4. 2001.

[3]   J. R. Davis, Davis & Associates, and ASM International, *ASM Specialty Handbook - Carbon and Alloy Steels*. 1996.

[4]   "Ducker Worldwide | Market Research, Strategy Consulting and Transaction Advisory." [Online]. Available: https://www.ducker.com/. [Accessed: 17-Jun-2019].

[5]   T. Lyman and H. E. Boyer, *Metals handbook*, 8th ed. Metals Park, Ohio: American Society for Metals, 1961.

[6]   A. Bouaïcha, "Étude de la fatigue d'un bras de suspension en alliage d'aluminium A357 semi-solide élaboré selon le procédé SEED," Université du Québec à Chicoutimi, 2012.

[7]   A. Saoudi, M. Bouazara, and D. Marceau, "Study of the fatigue life and weight optimization of an automobile aluminium alloy part under random road excitation," 2010.

[8]   K. A. RAGAB, A. BOUAICHA, and M. BOUAZARA, "Development of fatigue analytical model of automotive dynamic parts made of semi-solid aluminum alloys," *Trans. Nonferrous Met. Soc. China (English Ed.*, vol. 28, no. 6, pp. 1226–1232, 2018.

[9]   J. G. Kaufman and E. L. Rooy, *Aluminum Alloy Castings: Properties , Processes , and Applications.* 2004.

[10]   J. T. and G. D. St John, C. Caceres, D. Zhang, G. Edwards and Schaffe, "Aluminum alloys for cast automotive components," *Mater. Automot. Ind. Conf. Aust.*, 1996.

[11]   E. J. Vinarcik, *High Integrity Die Casting Processes*. 2002.

[12]   D. Kotecki, "Alloy and Temper Designation Systems for Aluminum and Aluminum Alloys," in *Advanced Materials and Processes*, vol. 155, no. 5, 1999, pp. 41–44.

[13]   A. A. (AA), "Aluminum Alloys 101 | The Aluminum Association." [Online]. Available: http://www.aluminum.org/resources/industry-standards/aluminum-alloys-101. [Accessed: 08-Mar-2018].

[14]   A. society of materials (ASM), *Science of Casting and Solidification. ASM handbook*. 2015.

[15] C. V.A.W., Hillier and Peter, *Hillier's Fundamentals of Motor Vehicle Technology*, 5th Editio. GreenGate Publishing Services, 2004.

[16] "Federal-Mogul," 2018. [Online]. Available: http://www.federalmogul.com/en-US/Pages/search.aspx?k=Hub+bearings&start=11. [Accessed: 03-Oct-2019].'

[17] A.Purushotham, "Comparative Simulation studies on McPherson Suspension System," *Int. J. Mod. Eng. Res.*, vol. 3, no. 3, pp. 1377–1381, 2013.

[18] J. R. Davis, *ASM Specialty Handbook: Aluminum and Aluminum Alloys*, vol. 1, no. August. 1993.

[19] M. Bouazara, A. Bouaicha, and K. A. Ragab, "Fatigue Characteristics and Quality Index of A357 Type Semi-Solid Aluminum Castings Used for Automotive Application," *J. Mater. Eng. Perform.*, vol. 24, no. 8, pp. 3084–3092, 2015.

[20] W. M. R. and D. L. Z. J. L. Jorstad, *Aluminum cast technolog*, 2nd ed. IL, USA: American Foundry Society, 2001.

[21] ASTM, "ASTM Standard B917/B917M 2008," in *Standard practice for heat treatment of aluminumalloy castings for all purpose*, 2008.

[22] B. S. S. and S. A. L. D.S. Thompson, ""Quench rate effects in Aluminum-ZincMagnesium- Copper alloys," *Metall. Trans.*, pp. 1149–1160, 1971.

[23] M. C. Flemings, "Semi-solid forming: the process and the path forward," *Metall. Sci. Technol.*, vol. 18, no. 2, pp. 3–4, 2000.

[24] W. . Winterbottom, "Semi-solid forming applications: high volume automotive products," *Technol. Gr. - AEMP Corp. - Jackson - Tennessee USA*, p. 6, 2000.

[25] S. Menargues, E. Martín, M. T. Baile, and J. A. Picas, "New short T6 heat treatments for aluminium silicon alloys obtained by semisolid forming," *Mater. Sci. Eng. A*, vol. 621, pp. 236–242, 2015.

[26] Y. Birol, "A357 thixoforming feedstock produced by cooling slope casting," *J. Mater. Process. Technol.*, vol. 186, no. 1–3, pp. 94–101, 2007.

[27] S. T. J.Wannasin, "Development of a semi-solid metal processing technique foraluminium casting applications," *Songklanakarin J. Sci. Technol*, no. 30 (2), pp. 215–220, 2008.'

[28] P. K. M. N. Mohammed, M. Z. Omar, M. S. Salleh, K. S. Alhawari, "Semisolid Metal Processing Techniques for Nondendritic Feedstock Production," *Sci. World J.*, p. 16,

2013.

[29] P. F. M. Chris S. Rice, "Slurry-Based Semi-Solid Die Casting," *Adv. Mater. Process.*, no. 159(10), 2001.

[30] G. Y. Liu, "Effect of Ageing Heat Treatment on the Hardness and Tensile Properties of Aluminum A356.2 Casting Alloy," 2009.

[31] H. Zhu, J. Guo, and J. Jia, "Correlation of the Aging Characteristics and Deformation Behavior of A357 Alloy," *ASM Int.*, vol. 10, no. April, pp. 186–191, 2001.

[32] K. Ragab, M. Bouazara, and X. Chen, "Influence of Thermal Aging Parameters on the Characteristics of Aluminum Semi-Solid Alloys," *Metals (Basel).*, vol. 8, no. 10, p. 746, 2018.

[33] S. D. Shinde, S. Maheshwari, and S. Kumar, "Literature review on analysis of various Components of McPherson suspension," *Mater. Today Proc.*, vol. 5, no. 9, pp. 19102–19108, 2018.

[34] M. Mahmoodi-Kaleibar, I. Javanshir, K. Asadi, A. Afkar, and A. Paykani, "Optimization of suspension system of off-road vehicle for vehicle performance improvement," *J. Cent. South Univ.*, vol. 20, no. 4, pp. 902–910, 2013.

[35] R. C. Hibbeler and Pearson Education, *Mechanics of Materials (8th edition).* 2013.'

[36] S. Hegazy, H. Rahnejat, and K. Hussain, "Multi-body dynamics in full-vehicle handling analysis," *Proc. Inst. Mech. Eng. Part K J. Multi-body Dyn.*, vol. 213, no. 1, pp. 19–31, 2000.

[37] X. Ning, C. Zhao, and J. Shen, "Dynamic analysis of car suspension using ADAMS/Car for development of a software interface for optimization," *Procedia Eng.*, vol. 16, pp. 333–341, 2011.

[38] Y. Zhisheng., *Automotive Theory: Machinery Industry Press*. 2006.

[39] M. Viqaruddin and D. Ramana Reddy, "Structural optimization of control arm for weight reduction and improved performance," *Mater. Today Proc.*, vol. 4, no. 8, pp. 9230–9236, 2017.

[40] A. Bouaïcha, "Étude de la fatigue et analyse du moulage d'un bras de suspension fabriqué en alliage d'aluminium semi-solide," Université du Québec à Chicoutimi, 2016.

[41] D. K. F, "Effect of small defects on the fatigue properties of medium strength cast

steel," *J Iron Steel Ins*, 1970.

[42] Y. Nadot and V. Denier, "Fatigue failure of suspension arm: Experimental analysis and multiaxial criterion," *Eng. Fail. Anal.*, vol. 11, no. 4, pp. 485–499, 2004.

[43] E. M. Elgallad, Z. Zhang, and X. G. Chen, "Effect of two-step aging on the mechanical properties of AA2219 DC cast alloy," *Mater. Sci. Eng. A*, vol. 625, pp. 213–220, 2015.

[44] K. A. Ragab, A. M. Samuel, A. M. A. Al-Ahmari, F. H. Samuel, and H. W. Doty, "Effect of multi-temperature aging on the characterization of aluminum based castings heat treated using fluidized bed technique," *Met. Mater. Int.*, vol. 19, no. 4, pp. 783–802, 2013.

[45] M. Abdulwahab, I. A. Madugu, S. A. Yaro, S. B. Hassan, and A. P. I. Popoola, "Effects of multiple-step thermal ageing treatment on the hardness characteristics of A356.0-type Al-Si-Mg alloy," *Mater. Des.*, vol. 32, no. 3, pp. 1159–1166, 2011.

[46] P. Gauthier, "Corrosion behaviour study of the forged AA6082 aluminum alloy from different feedstock.," 2010.

[47] T. R. Prabhu, "Effects of ageing time on the mechanical and conductivity properties for various round bar diameters of AA 2219 Al alloy," *Eng. Sci. Technol. an Int. J.*, vol. 20, no. 1, pp. 133–142, 2017.

[48] J. Kim, E. Yim, C. Jeon, C. Jung, and B. Han, "Fatigue Life Prediction of a Rubber Material Based on Dynamic Crack Growth Considering Shear Effect H.," *Int. J. ...*, vol. 13, no. 2, pp. 293–300, 2012.

[49] C. J. Davidson, J. R. Griffiths, M. Badiali, and A. Zanada, "Fatigue properties of a semi-solid cast Al-7Si-0 . 3Mg-T6 alloy," vol. 18, no. 2, 2000.

[50] Y. X. Gan and R. A. Overfelt, "Fatigue property of semisolid A357 aluminum alloy under different heat treatment conditions," *J. Mater. Sci.*, vol. 41, no. 22, pp. 7537–7544, 2006.

[51] K. A. Ragab, M. Bouazara, A. Bouaicha, and O. Allaoui, "Microstructural and mechanical features of aluminium semi-solid alloys made by rheocasting technique," *Mater. Sci. Technol.*, vol. 33, no. 6, pp. 646–655, 2017.